Performance Analysis of NOMA Enhanced Backscatter Communication for Green IoT Networks

By

Ahsan Waleed Nazar

Fall 2018-MS(EE-24)-00000101076

Supervisor

Dr. Syed Ali Hassan

Department of Electrical Engineering

A thesis submitted in partial fulfillment of the requirements for the degree of MS in Electrical (Telecommunication) Engineering

In

Military College of Signals,

National University of Sciences and Technology (NUST),

Islamabad, Pakistan.

(August 2020)

Approval

It is certified that the contents and form of the thesis entitled "**Performance Analysis of NOMA Enhanced Backscatter Communication for Green IoT Networks**" submitted by **Ahsan Waleed Nazar** have been found satisfactory for the requirement of the degree.

Advisor: **Dr. Syed Ali Hassan**

Signature: _____

Date: _____

Committee Member 1: **Dr. Muhammad Imran**

Signature: _____

Date: _____

Committee Member 2: **Dr. Adil Masood Siddiqui**

Signature: _____

Date: _____

Committee Member 3: **Dr. Alina Mirza**

Signature: _____

Date: _____

Abstract

Backscatter communication (BackCom) has been emerging as a prospective candidate in tackling lifetime management problems for massively deployed Internet-of-Things devices, which suffer from battery related issues, i.e., replacements, charging, and recycling. This passive sensing approach allows a backscatter sensor node (BSN) to transmit information by reflecting the incident signal from a carrier emitter without initiating its transmission. To multiplex multiple BSNs, power-domain non-orthogonal multiple access (NOMA), which is a prime candidate for multiple access in beyond 5G systems, is fully exploited in this work. Recently, considerable attention has been devoted to the NOMA-aided BackCom networks in the context of outage probabilities and system throughput. However, the closed-form expressions of bit error rate (BER) for such a system has not been studied. In this paper, we present the design and analysis of a NOMA enhanced bistatic BackCom system for a battery-less smart communication paradigm. Specifically, we derive the closed-form BER expressions for a cluster of two devices in a bistatic BackCom system employing NOMA with imperfect successive interference cancellation under both fading-free and Nakagami-m fading channel condition. The obtained expressions are utilized to evaluate the reflection

coefficients of devices needed for the most favorable system performance. Our results also show that NOMA-BackCom achieves better data throughput compared to the orthogonal multiple access-time domain multiple access schemes (OMA-TDMA).

Dedication

I dedicate this thesis to my mother for her valuable support throughout my life and my nieces: Mahveen, Eshal and Zoha for not letting me get bored during the research work.

Certificate of Originality

I hereby declare that this submission is my own work and to the best of my knowledge it contains no materials previously published or written by another person, nor material which to a substantial extent has been accepted for the award of any degree or diploma at NUST MCS or at any other educational institute, except where due acknowledgement has been made in the thesis. Any contribution made to the research by others, with whom I have worked at NUST MCS or elsewhere, is explicitly acknowledged in the thesis.

I also declare that the intellectual content of this thesis is the product of my own work, except for the assistance from others in the project's design and conception or in style, presentation and linguistics which has been acknowledged.

Author Name: **Ahsan Waleed Nazar**

Signature: _____

Acknowledgment

I would like to thank Allah Almighty for His blessings on me to carry out this research work. Secondly, I would like to extend my sincere gratitude to my supervisors, Dr. Syed Ali Hassan and Dr. Muhammad Imran, for their constant support throughout my research. Special thanks to my primary supervisor, Dr. Syed Ali Hassan, who provided valuable technical guidance and constructive suggestions on my research works and directions. His wide experience, inspiring research methodology and enthusiasm in dealing with complex problems will have a profound effect on my future carreer. He introduced me to the world of research and everything I know I owe it to him. Finally, I would like to thank my most supportive and helping friends Shahjahan, Junaid and Qasim, my friends from MCS and Waseem, Ismaeel and Shahzeb from my IPT Research Lab, as without their encouragement and guidance, I would not have been able to achieve what I have thus so far.

Table of Contents

List of Figures

List of Tables

List of Abbreviations

IoT	Intenet-of-Things
NOMA	Non-orthogonal multiple access
OMA	Orthogonal multiple access
PD-NOMA	Power domain-non-orthogonal multiple access
BSN	Backscatter sensor node
BSR	Backscatter sensor reader
mMTC	Massive machine type communications
eMBB	Enhanced mobile broadband
URLLC	Ultra-reliable and low latency communications
BackCom	Backscatter Communication
MoM	Method of moments
K-S	Kolmogorov-Smirnov
BER	Bit error rate
CE	Carrier emitter

PDF	Probability density function
TDMA	Time division multiple access
BPSK	Binary phase shift keying
BBCS	Bistatic BackCom system
CW	Continuous wave

Chapter 1

Introduction and Background to Thesis

In this chapter, we give a brief overview and background of Internet-of-things (IoT) enabling technology, i.e., fifth-generation (5G) wireless networks before introducing the motivation for studying the backscatter communication (BackCom) systems in this thesis. We shall also discuss the non-orthogonal multiple access (NOMA) scheme and its advantages compared to the orthogonal multiple access (OMA) scheme.

1.1 Overview of 5G

The past few years have seen dramatic growth in the employment of wirelessly networked devices which has all been made possible due to great advances and innovations in the field of wireless communications. In particular, the advancements in wireless communications has led to massive growth in the

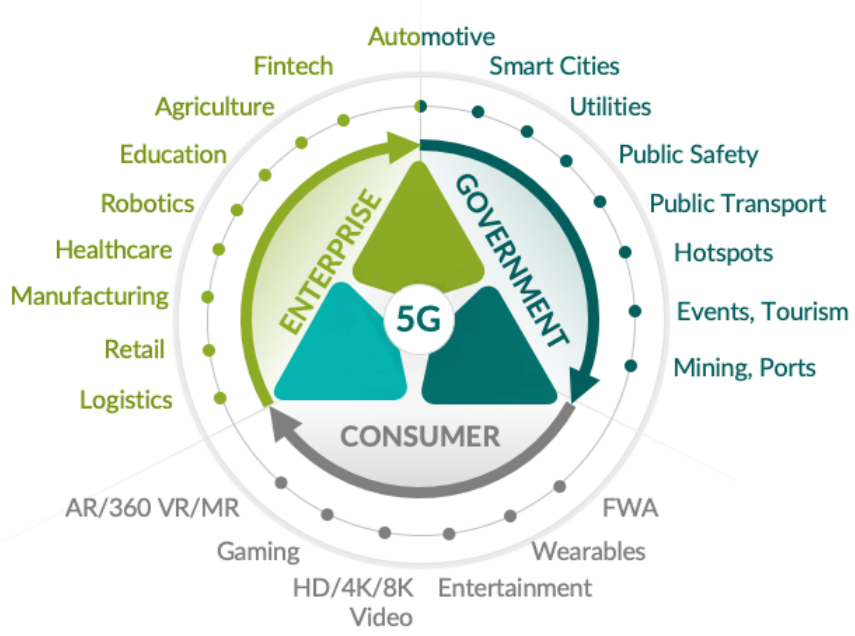

Figure 1.1: Usage of 5G in various applications.

number of wireless communication devices and sensors for emerging applications. These networked devices, specifically IoT, have enabled great ease in the domains of both consumer and industrial applications. The next big thing for connectivity is the arrival of 5G which is expected to provide a substantial breakthrough by providing 1000 times higher system capacity, 10 times higher spectrum efficiency connecting at least 100 billion devices, 10 times lower system latency, and 10 times lower energy energy-per-bit usage as compared to the 4G networks [2–6]. Fig 1.1 shows some of the 5G applications.

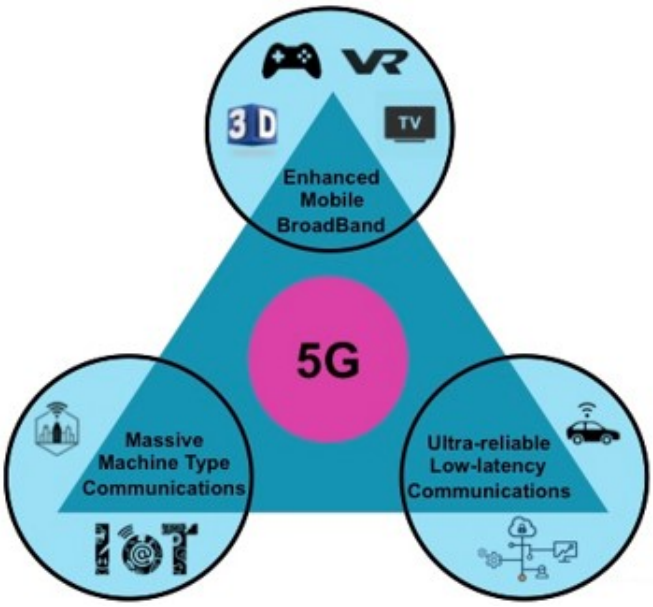

Figure 1.2: 5G services categories and use cases in IMT 2020 [1].

1.1.1 5G Network Services

5G is envisioned to provide the following three service usage scenarios which are expected to revolutionize our daily life [7–9]:

- Enhanced mobile broadband (eMBB): 5G network is expected to provide significantly faster data speeds and wide-area coverage and high mobility to end-users. Its applications include services that have high requirements for bandwidth, such as 4k videos, augmented reality (AR), and virtual reality (VR).

- Massive machine-type communications (mMTC): This service is for mMTC deployment of IoTs that will connect billions of devices or sensors placed in a relatively smaller area. Its applications include smart city and smart agriculture. These devices have low cost, long battery

life, and delay insensitive data.

- Ultra-reliable and low latency communications (URLLC): This service is for those applications which have strict latency and reliability requirements. There is a wide range of applications usage cases that have such stringent requirements such as factory automation, tactile internet, remote medical care, and automated driving as shown in Fig. 1.2.

1.1.2 IoT

IoT is an exciting outcome of the next-generation 5G networks which will provide the above-mentioned services for various use cases. IoT allows devices and humans to communicate with each other and act as a bridge between a physical and cyber world connected through the internet ready for remote control and monitoring. The IoT is the next big technological advancement the world has ever seen since the deployment of the Internet in the late 1960s [10]. The proliferation of billions of smart sensors and actuators connected with the internet will enable human beings and computers to acquire knowledge about the world we live in and interact with it too. This rise in devices necessitates new technology paradigms for providing massive connectivity, low latency and reliable service to fulfill IoT requirements in smart application [11–13]. mMTC is envisaged to provide a leading role to cater to this requirement [14].

The IoT proliferation in the context of massive machine type communication (mMTC) is one of the key technology trends driving the fifth-generation

(5G) networks innovation [15]. IoT cellular devices connectivity is expected to reach 5.0 billion devices by 2025 because of its immense applicability in the smart home, smart city, smart agriculture, connected health, smart industries, autonomous vehicles, and unmanned aerial vehicles (UAVs) [16]. For instance, in smart cities, an IoT network can provide efficient waste management, parking assistance, and air quality monitoring. Similarly, in smart agriculture, such an IoT network can be used to monitor soil moisture, pest control mechanisms, and livestock tracking [17], [18].

1.2 Energy Efficiency Concerns

Energy-efficient communications have become an important focus in both academia and industry due to the exponential growth of these devices coupled with growing demands of energy [19]. It is expected that by 2025 the communications industry will be responsible for 20% of all the world's electricity [20]. Therefore, research in energy-efficient wireless communications is critical to strike a balance between energy consumption and system performance. It is understood that the communication phase takes many times more power as compared to the detection or sensing phase of the smart device. The existing solutions use Marconi-type radio for wireless connectivity, such as Bluetooth, 802.11, ZigBee, LoRa etc. These radios are usually energy consuming and expensive owing to the active radio-frequency (RF) transmission components. Fig. 1.3 shows the comparison of the energy consumption of the communication and sensing phase.

Power-efficient wireless connectivity is at the heart of the massive prolifer-

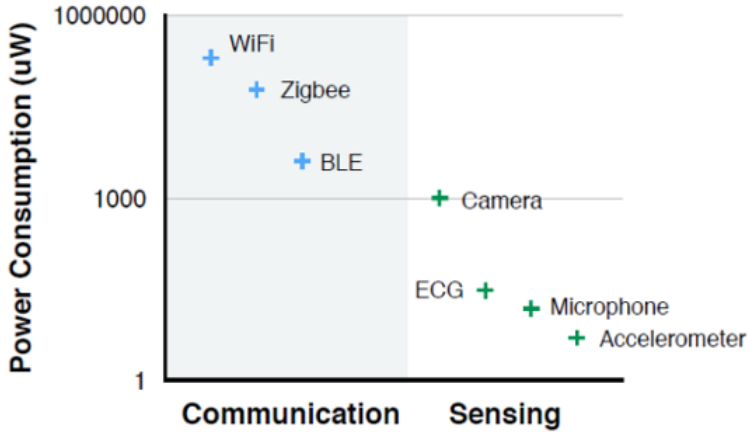

Figure 1.3: Wireless radios consume an order of magnitude higher power compared to low power sensors.

ation of Internet-of-thing (IoT) networks for wide-scale and fine-grained sensing and control in various domains. For instance, IoT networks of constrained battery-operated devices are attractive for applications in both the consumer and industrial domains, e.g., smart home/city/agriculture, e-health, building/industrial- automation, and vehicular/aerial networks [15]. This pervasiveness and usability of IoT connectivity are equally reflected in currently connected IoT devices, which will further be reaching 24.5 billion devices by 2025 [21]. In this expected scenario, managing the network lifetime becomes critical, especially when the conventional battery-based solutions are not viable due to the high cost of battery replacements and recycling concerns. In particular, battery recharging/replacement is challenging in cases where most of the sensors are hidden (e.g., inside concrete walls) or deployed in an inaccessible environment (e.g., under cultivated land). As a result, various energy harvesting techniques are under investigation to overcome this challenge [17]. However, not all forms of energy harvesting solutions, i.e.,

light, kinetic or thermal, are suitable for a low cost sensor, and we have to rely on radio-frequency (RF) energy harvesting due to its many attractive characteristics.

1.3 Backscatter Communications

Recently, for massive IoT networks, backscatter communication (BackCom) has emerged as one of the promising radio-frequency (RF) energy harvesting techniques, which enables communication without battery backup [22] [23]. The low-complexity and low-power BackCom technique allows backscatter sensor nodes (BSNs) to communicate with a backscatter sensor reader (BSR) by passive reflection from a carrier emitter (CE) and modulation without requiring any active RF transmission component. It is based ion the concept that instead of using active RF components to communicate, a continuous wave (CW) signal is is generated centrally and is used to illuminate multiple nodes.

A BackCom system is generally composed of three components, a carrier emitter (CE), a backscatter sensor reader (BSR), and backscatter sensor nodes (BSNs). The BSN is not equipped with an active RF transmission component for information transfer rather it relies on the unmodulated carrier signal transmitted by the CE for both energy harvesting and backscatter. This backscatter is made possible because of the intentional impedance mismatch at the antenna input which results in different reflection coefficients [24]. Data encoding for backscatter over an incident wave is carried out by varying the reflection coefficients at the antenna input side. This

backscatter approach is vastly different from the generally applied wireless harvesting approach where nodes first harvest energy to perform active RF transmission. Thus, transmissions in a backscatter communication consume orders of magnitude less energy than a typical radio and the absence of an active RF component in BSNs enables simpler and low complexity circuits. Therefore, the BackCom approach is most suitable for IoT networks [25].

1.3.1 BackCom Basics

The BackCom works on the principle of reflection of incident CW signal by backscatter tags and by modifying and modulation the signal for secondary transmission, i.e., backscatter. This modulation and reflection is made possible by the impedance mismatch. On a BSN there are two impedances: antenna impedance (Z_A) and load impedance (Z_L). By changing the value of these impedances, reflection coefficient Γ of the backscatter tag is changed and it is given by [26]

$$\Gamma = \frac{Z_L - Z_A}{Z_L + Z_A} = 1 - \frac{2\,|Z_A|}{|Z_A| + |Z_L|\,e^{-j(\theta_A - \theta_L)}} = |\Gamma|\,e^{j\theta_T}, \tag{1.1}$$

where θ_A and θ_L are the phases of the antenna and load impedances. The magnitude and phase of Γ is given by

$$|\Gamma_T| = \frac{|Z_A|^2 + |Z_L|^2 - 2\,|Z_A|\;|Z_L|\,\cos(\theta_A - \theta_L)}{|Z_A|^2 + |Z_L|^2 + 2\,|Z_A|\;|Z_L|\,\cos(\theta_A - \theta_L)}, \tag{1.2}$$

$$\theta_T = \arctan\left(\frac{2\,|Z_A|\;|Z_L|\,\sin(\theta_A - \theta_L)}{|Z_A|^2 - |Z_L|^2}\right). \tag{1.3}$$

The reflection coefficient is the ratio of the complex amplitudes of the incoming signal $S_{\text{in}}(t)$ and the reflected signal $S_{\text{out}}(t)$. Let the incoming sine wave signal be

$$S_{\text{in}}(t) = A_{\text{in}} e^{j(2\pi f_{\text{in}} t + \theta_{\text{in}})}. \tag{1.4}$$

By using the definition of reflection coefficient, the reflected signal $S_{\text{out}}(t)$ is given by

$$S_{\text{out}}(t) = \Gamma \cdot S_{\text{in}}(t) = |\Gamma| A_{\text{in}} e^{j(2\pi f_{\text{in}} t + \theta_{\text{in}} + \theta_T)}. \tag{1.5}$$

Therefore, by controlling the complex value of the reflection coefficient Γ, which in itself is derived from the complex values of antenna and load impedances, i.e., Z_A and Z_L, we can modify or modulate the value of the reflected signal $S_{\text{out}}(t)$.

1.3.2 BackCom Arhcitecture Types

BackCom can be classified into three types based on their architectures [27], [28]:

- *Monostatic Backscatter Communications Systems:* In this type of BackCom system, there are two main components, i.e., a backscatter transmitter ,e.g., an RFID tag, and a reader as shown in Fig. 1.4(a). The reader is responsible for both transmitting the CW signal for backscattering and decoding the reflected signal. It incorporates an RF source and a backscatter receiver. As the RF source and the backscatter re-

ceiver are placed on the same device, i.e., the tag reader, the modulated signals may suffer from a round-trip path loss. Moreover, the system can be affected by the doubly near-far problem. It is mainly used for short-range communication.

- *Bistatic Backscatter Communications Systems:* Different from the Monostatic BackCom, in this type of system, the RF source, i.e. carrier emitter, is decoupled from the backscatter receiver. Its architecture is shown in Fig. 1.4(b). Such type of system can avoid the round trip path loss problem as was the case with Monostatic system. Additionally, the performance of the system can be improved immensely by strategically placing the carrier emitters around the field. Specifically, one centralized backscatter receiver can be located in the field while multiple carrier emitters are well placed around backscatter transmitters. It will result in increased coverage of the BackCom system. This will also result in cheap deployment of the system as the development cost of carrier emitters and backscatter receivers of Bistatic is cheaper than that of Monostatic backscatter systems due to the simple design of the components.

- *Ambient Backscatter Communications Systems:* This architecture is similar to the Bistatic one where the carrier emitters are separated from the backscatter reader. But they use ambient RF sources, e.g., TV towers, cellular base stations, and Wi-Fi APs instead of using dedicated RF sources as in Bistatic architecture. This is shown in 1.4(c).This approach affords some advantages compared with Bistatic approach.

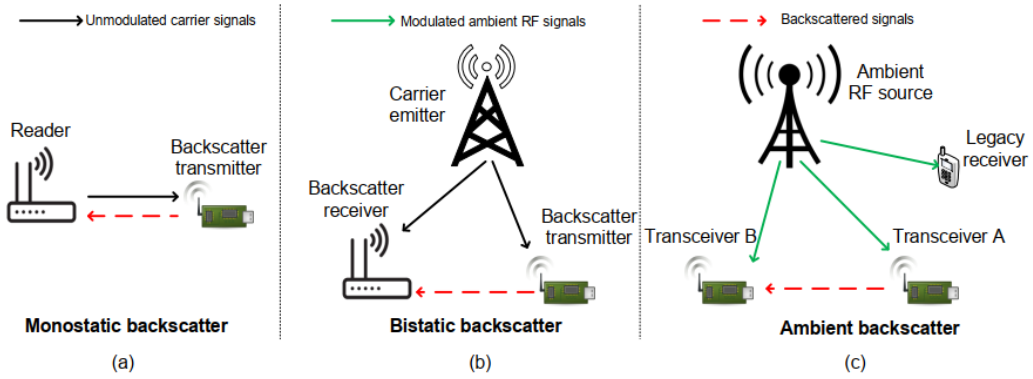

Figure 1.4: BackCom Arhcitecture Types.

First, because of using already-available RF sources, there is no need to deploy and maintain dedicated RF sources, thereby reducing the cost and power consumption. Second, by utilizing existing RF signals, there is no need to allocate a new frequency spectrum, and the spectrum resource utilization can be improved. However, it also has some inherent disadvantages. First, it is not a reliable source for RF energy harvesting and is not under designer control. Secondly, it can act as direct interference to BackCom receiver as opposed to a CW transmission in Bistatic scheme.

1.4 Non-orthogonal multiple access (NOMA)

With the massive increase in wireless devices, there is a growing concern for limited resources and media arbitration. The traffic over the wireless medium is expected to increase by 1000 folds in the next decade. To overcome these challenges, a great deal of research is being carried out on multiple access schemes for future networks. Until now, several techniques such as time, fre-

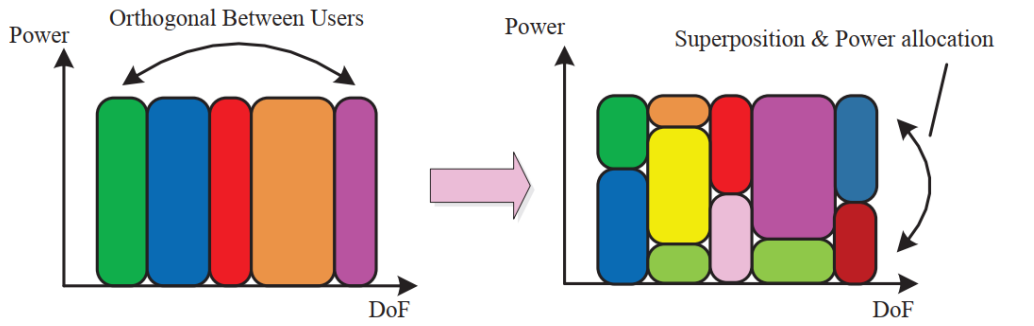

Figure 1.5: From OMA to NOMA via power domain multiplexing.

quency, and code division multiplexing have been used collectively known as Orthogonal multiple access (OMA) schemes. Orthogonal frequency division multiplexing (OFDM) is also being used to serve several users with reduced interference offering high spectral efficiency. A single user is served in a single orthogonal resource block in these techniques as shown in Fig. 1.5 which becomes spectrally inefficient if some bandwidth resources are allocated to a user with bad channel conditions. The need for future massive and high capacity encompasses high connectivity, reliability, ultra-low latency, improved fairness, and high throughput.

In contrast to conventional OMA, NOMA transmission techniques intend to share a DoF among users via superposition and consequently need to employ multiple user detection (MUD) to separate interfered users sharing the same resource block as shown in Fig. 1.5. Recently, non-orthogonal multiple access (NOMA) is envisaged as an essential enabling technology for 5G wireless networks, especially for uncoordinated transmissions. it exploits the channel differences between a strong and a weak user to its advantage. By allowing multiple users to be served in the same resource block (to be decoded

using successive interference cancellation (SIC)), NOMA may greatly improve the spectrum efficiency and may outperform traditional orthogonal multiple access schemes in many scenarios. Further, it is suitable for mMTC, since it supports a large number of users to be served simultaneously. The users also experience low latency, as due to simultaneous transmissions, the user does not need to wait for its resource block, i.e., time slot. NOMA can also maintain user-fairness and diverse quality of service by flexible power control between the strong and weak users; particularly, as more power is allocated to a weak user, NOMA offers higher cell-edge throughput and thus enhances the cell-edge user experience. NOMA is usually divided into two types:

- *Power-domain NOMA:* In this, signals of different users are superimposed upon each other after channel coding and modulation, i.e., they use the same time-frequency resource block but differentiated by the power accorded to different users. This aggregate signal is decoded at the receivers by using SIC. This results in an increased in spectral efficiency at the cost of the increased receiver complexity. Based on the results from information theory, the non-orthogonal multiplexing using superposition coding at the transmitter and SIC at the receiver is the most optimal in acheiving the capacity regions of broadcast channels.

- *Code-domain NOMA* In this, the user share the same resource block but is differentiated by the different spreading sequences like in code-division multiple access (CDMA) systems.

In this thesis, we will employ uplink power-domain NOMA as the multiple access scheme.

1.5 Thesis Motivation

The motivation of this thesis is to study the design and perform analysis of a NOMA enhanced bistatic BackCom system for a battery-less smart communication paradigm employed in an IoT scenario under AWGN and Nakagami fading channels. No concrete literature exists which studies the problem of evaluating the BER in such a communication system which is necessary to carry out the reliability analysis and to find out the suitable reflection coefficients for the backscatter tags to fulfill the QOS requirement. For this purpose, we derive the analytical closed-form BER equations and validate it by performing Monte Carlo simulations.

1.6 Thesis Contribution

The thesis work presents the following main contributions:

- We propose a NOMA enhanced bistatic BackCom system for battery-less smart communication among BSNs, where the reflection coefficients of BSNs can be manipulated to achieve better system performance in terms of effective data bits.

- The BER performance of a NOMA enhanced bistatic BackCom system, impaired by both, an AWGN and a Nakagami-m fading channel, with practical impairements such as imperfect SIC is considered, where approximate closed-form analytical BER expressions of binary phase-shift keying (BPSK) are derived for two BSNs. The derived BER expressions are verified by Monte Carlo simulations for various reflection

coefficients.

- The probability density functions (PDFs) of the sum and difference of two independent and non-identically distributed (i.n.i.d) Nakagami-m distributions has not been derived in literature before. It is shown with the help of some statistical approaches such as the moment matching method that it follows Nakagami and normal distribution respectively and we derive the average BER expressions under such a scenario.

- The increase in effective non-erroneous transmitted bits over a large period in a NOMA-BackCom scheme is compared with an OMA scheme for a variety of reflection coefficient conditions. It is shown that NOMA-BackCom outperforms the OMA-TDMA scheme by multiplexing the BSNs.

- Our results suggest that at relatively higher transmit SNRs, system performance can be greatly improved by setting suitable reflection coefficients rather than an increment in transmit power of the CE.

- The derived expressions allow us to investigate the effect of reflection coefficients on the performance of the NOMA-BackCom system and to roughly figure out the optimal reflection coefficients.

1.7 Thesis Organization

The organization of the thesis is presented as follows. Chapter 2 highlights the literature review of the important concepts proposed in this thesis for

providing a flow for the readers. In Chapter 3, we carry out the performance analysis of NOMA enhanced BackCom system over an AWGN channel. System model over and AWGN channel is developed and closed-from analytical equations are derived. In Chapter 4, we present the numerical and simulation results and find out the effect of various reflection coefficients on the BER of each user. In Chapter 5, we develop a detailed system model for a bistatic BackCom system aided by NOMA under a Nakagami-m fading channel. We use methods of moments (MOM) to derive the BER expressions to qualify the system performance under different scenarios. In Chapter 6, we show the numerical and simulation results and identify the range of reflection coefficients necessary for required system performance. Finally, chapter 6 presents the conclusions and further proposes the future work

Chapter 2

Literature Review

In this section, we highlight the drivers and challenges related to adopting NOMA enchanced backscatter communication system and put some light on the work done in the related field. The basic concepts and related literature of BackCom system and NOMA have already been covered in the previous chapter. In this chapter, we will touch on the research work recently carried out while incorporating the two. The backscatter technique implementation for passive IoTs has been limited due to its inherent short-range communication. Recently, the BackCom system has been suggested for overcoming this limitation using bistatic architectures [29], [30]. In bisatic architecture, the CE and BSR are not co-located, therefore, it allows setting up a more flexible network topology which can also mitigate the near-far effect [31].

Non-orthogonal multiple access (NOMA), because of its low latency and high spectral efficiency, is the ideal candidate to support a large number of IoT nodes in a BackCom uplink communication system [32]. Recently, NOMA-aided BackCom has proven to be a key technology for collating data

from multiple BSNs [33], [34]. In [35], the authors investigated the performance of a NOMA-enhanced BackCom system, and the significance of adopting NOMA with the BackCom system was demonstrated by analyzing the average number of successfully decoded bits. Similarly, the authors in [36–38] and [39] evaluated the performance of NOMA-aided BackCom network in terms of outage probability and system throughput. The authors in [40] and [41] studied the problem of resource allocation in NOMA-enhanced BackCom networks. In [42], the authors analyzed the outage probabilities and the ergodic rate for a symbiotic system that integrates cellular NOMA and ambient BackCom in an IoT network. The authors in [43] studied the optimal time allocation policies of a power station-powered BackCom system for a hybrid NOMA-TDMA scheme. Relay assisted BackCom system has been studied in [44]. In [45], the authors proposed a NOMA-BackCom application in unmanned aerial vehicle (UAV) based data collection with optimized UAV altitude and trajectory.

Based on the aforementioned literature survey, to the best of authors' knowledge, there is no reported work that carries out the BER performance analysis of uplink NOMA in a BackCom system, which is an essential component in system design and optimization. In this work, we consider a NOMA-enhanced bistatic backscatter uplink communication under the Nakagami-m fading channel where one reader serves a cluster of randomly deployed BSNs. To maintain low NOMA decoding complexity, BSNs are usually divided into a cluster of two users. The reflection coefficients of the BSNs are set different from each other to make the wireless channel distinct to better exploit power-domain NOMA. The proposed scheme results in an increase in effec-

tive non-erroneous transmitted bits as compared to an OMA scheme.

Chapter 3

NOMA-BackCom Systems in AWGN Channel

3.1 System Model

In this chapter, we consider the case of a single backscatter reader and a single cluster consisting of two semi-passive BNs. The BNs do not effectively transmit any radio signal, instead, the reader sends a continuous wave (CW) signal to the BNs. After energy harvesting to support the operations of sensing and micro-controller, the BNs reflect the incident CW signal to achieve communication with the reader. This backscatter is carried out by modulating the incoming signal using variable impedance. Due to the energy and complexity constraints of a BackCom system, BPSK modulation is considered in this work, where the modulation is performed by changing the load impedance between two impedance states through a micro-controller. These two impedance states correspond to the same magnitude but with two

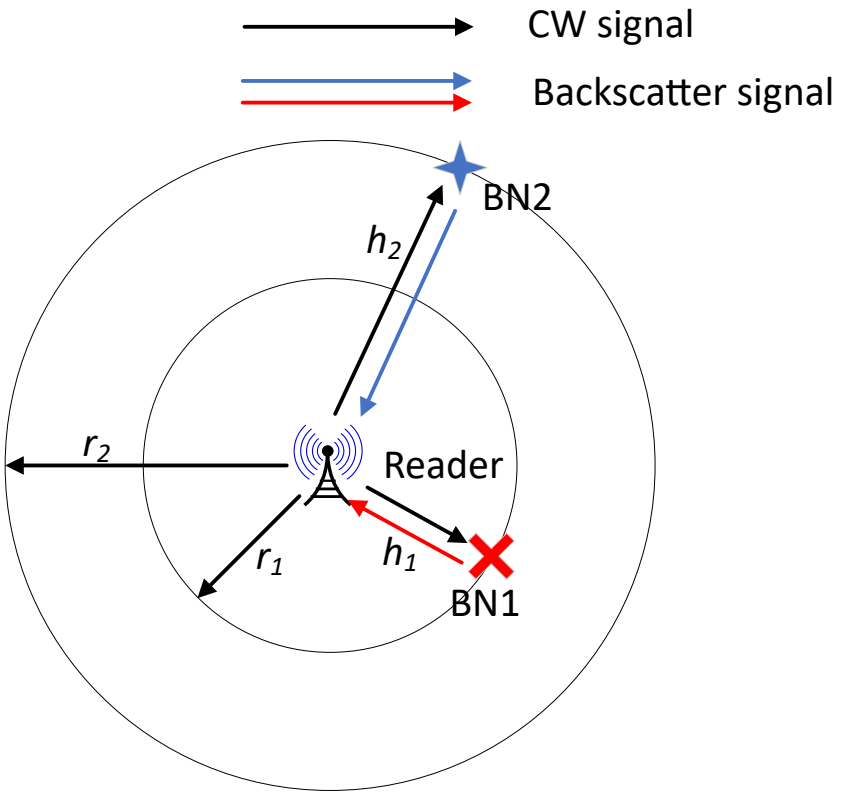

Figure 3.1: Illustration of uplink NOMA-BackCom system

different phase shifts.

An uplink NOMA scheme is utilized in this system, whereby, both BNs reflect the incoming signal by sharing the same time-frequency resource. The received signal at the reader undergoes double attenuation effects due to dyadic channel from reader to the BNs and back. Fig. 3.1 illustrates the corresponding schematic of the uplink NOMA scheme. The received signal at the reader is given by

$$y = \sqrt{P_r \xi_1} h_1 x_1 + \sqrt{P_r \xi_2} h_2 x_2 + w, \tag{3.1}$$

where ξ_i $(i \in \{1, 2\})$ and h_i denote the power reflection coefficient of

BNs and channel coefficients between the BNs and the reader. Because of the small coverage region of a BackCom system, a strong line-of-sight (LOS) link is assumed between the reader and the BNs and, therefore, a path loss-only channel model is considered which consists of the double attenuation effect (i.e., $r_i^{2\alpha}$, where r_i denote the distance between the reader and the i-th BN and α is the path loss exponent). In (5.1), P_r is the reader transmit power, x_i is the BPSK modulated information signal of user i, and w is additive white Gaussian noise (AWGN) with zero mean and N_0 variance.

A successive interference cancellation (SIC) process is implemented at the reader to decode the two users' signals. For uplink NOMA, the optimal order of decoding is in the order of decreasing channel gains and it is assumed in our study that $|h_1|^2 > |h_2|^2$. Because of stronger channel conditions, the signal from user 1, u_1, is decoded first by treating user 2, u_2, as inter-user interference (IUI) at the reader. Next, u_2 signal is decoded after subtracting the detected u_1 symbol from received composite signal y. If u_1's signal is decoded correctly then no IUI is faced in decoding of u_2, otherwise, there will be error propagation from u_1 when decoding u_2. In conventional power-domain NOMA, the multiplexed devices can transmit with different powers to accrue maximum benefit from NOMA. However, in a BackCom system, owing to no active RF transmission capability, the BNs reflect with different reflection coefficients to imitate similar behavior. Therefore, it is instinctive that we set the reflection coefficient for the two users as distinct as possible to aid in the NOMA process. Accordingly, ξ_1 is set as large as possible while, ξ_2 is set as small as possible. In this scenario, the signal to noise ratio (SNR) of the two users are defined as $\text{SNR}_1 = P_r\xi_1|h_1|^2/N_0$ and $\text{SNR}_2 = P_r\xi_2|h_2|^2/N_0$.

3.2 NOMA-BackCom BER Performance Analysis

In this section, we mathematically derive the closed-form expressions of the BER for the two BNs. Assume $2d\sqrt{\xi_1}$ $(d > 0)$ as the minimum distance between received constellation points of u_1 without AWGN. The relation between the minimum signal distance $2d$ and the bit energy ε_b can be expressed as [46]

$$d_{min} = \sqrt{\left(\log_2 M \times \sin^2 \frac{\pi}{M}\right) \varepsilon_b} \quad . \tag{3.2}$$

For binary phase-shift keying (i.e., $M = 2$), $d = \sqrt{\varepsilon_b}$. As the signal of u_2 is superimposed on u_1 at the reader, therefore, the minimum distance between received constellation points of u_2 without AWGN is $2d\sqrt{\xi_1}/\sqrt{R}$ where R is the ratio of SNR_1 and SNR_2, i.e., $R = (\xi_1 |h_1|^2)/(\xi_2 |h_2|^2)$.

By virtue of its strong channel condition, u_1 is decoded first. Fig. 3.2 shows the constellation diagram of the composite signal received at the backscatter reader. As noted from (5.1), the received signal y is a superposition of two BPSK modulated information signals of two BNs, where each constellation point is represented by two bits (a_1, a_2). Here, a_1 is the BPSK bit of u_1 and a_2 is the BPSK bit of u_2. Because of the presence of IUI from u_2, a_1 is translated into two possible constellation points. The shaded block shows the two possible values that a particular u_1 bit may take due to IUI. Moreover, it is assumed that all symbols have an equal prior probability of transmission.

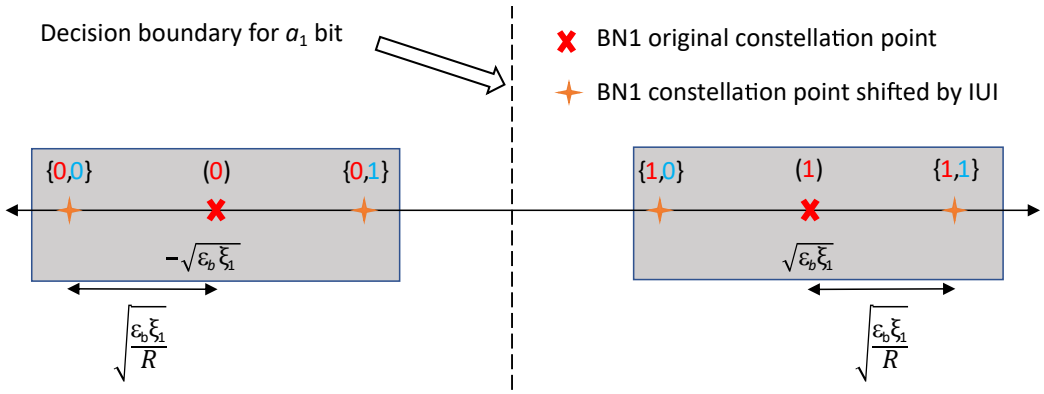

Figure 3.2: The received signal space diagram for u_1(red color and blue color represent u_1 and u_2 BPSK bit, respectively)

3.2.1 BER of the First User

For a_1, the decision boundary for bit detection is represented by the dotted line in Fig. 3.2 and there are four possible cases (represented by four orange stars) in which bit a_1 can be decoded incorrectly. When (0,0) is sent, the decision boundary is at a distance of $\sqrt{\varepsilon_b \xi_1} + \sqrt{\varepsilon_b \xi_1 / R}$ from constellation point and if the AWGN exceeds this value, a bit error will occur due to wrong decoding of a_1. By following the same procedure for three other points, the probability that a_1 is in error is

$$P_1(e) = \frac{1}{4}\left[\operatorname{erfc}\left(\frac{\sqrt{\varepsilon_b \xi_1} + \sqrt{(\varepsilon_b \xi_1)/R}}{\sqrt{N_0}}\right) + \operatorname{erfc}\left(\frac{\sqrt{\varepsilon_b \xi_1} - \sqrt{(\varepsilon_b \xi_1)/R}}{\sqrt{N_0}}\right)\right], \tag{3.3}$$

where erfc(.) is the complementary error function.

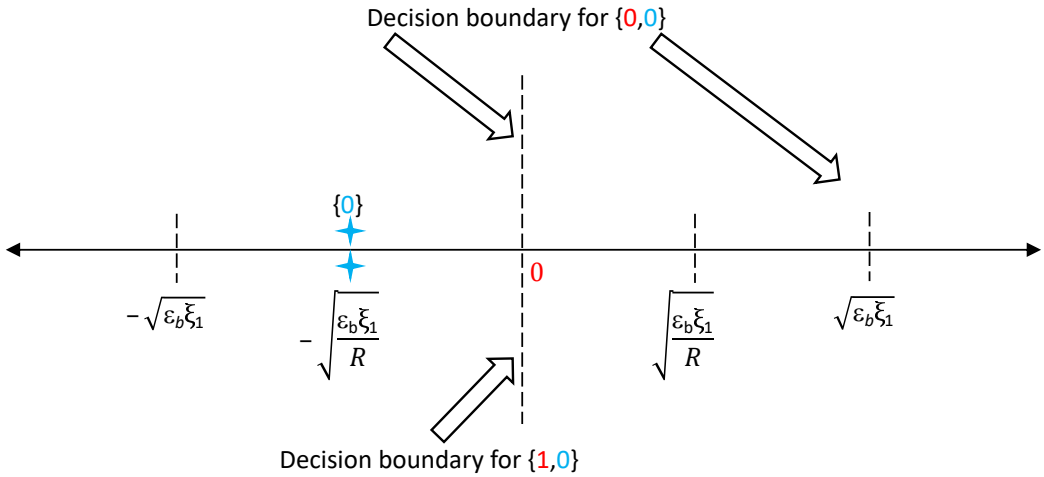

Figure 3.3: Signal space diagram for u_2 with correct u_1 for (0,0) and (1,0)

3.2.2 BER of the Second User

For decoding of u_2 bit a_2, SIC process is implemented, whereby, u_1 reconstructed bit, $\hat{a_1}$, is subtracted from received aggregate signal y. Therefore, the decoding of a_2 depends on the decoding result of a_1. This can be divided into two cases; case I: correct decoding of a_1 and case II: wrong decoding of a_1.

Fig. 3.3 shows the constellation diagram of a_2 when a_1 has been correctly decoded (i.e., case I). For decoding of bits {0,0} when a_1 has been correctly decoded, it can be observed from Fig. 3.2 that the noise must be less than $\sqrt{\varepsilon_b\xi_1} + \sqrt{(\varepsilon_b\xi_1)/R}$. Whereas, for incorrect decoding of a_2, as shown in Fig. 3.3, the noise must exceed $\sqrt{(\varepsilon_b\xi_1)/R}$. Therefore, the decision boundaries for a_2 in case I are $\sqrt{(\varepsilon_b\xi_1)/R}$ and $(\sqrt{\varepsilon_b\xi_1} + \sqrt{(\varepsilon_b\xi_1)/R})$. A bit error in a_2 will occur if AWGN falls within these boundaries.

For decoding {1,0}, it can be seen from Fig. 3.2 that AWGN should exceed $(-\sqrt{\varepsilon_b\xi_1} + \sqrt{(\varepsilon_b\xi_1)/R})$ for correct decoding of a_1. Similarly, as

illustrated in Fig. 3.3, for incorrect a_2 decoding, AWGN should exceed $\sqrt{(\varepsilon_b\xi_1)/R}$. Therefore, the decision boundary of a_2 for decoding {0,1} in case I is $\sqrt{(\varepsilon_b\xi_1)/R}$. A bit error in decoding u_2 will occur whenever AWGN shall exceed this boundary.

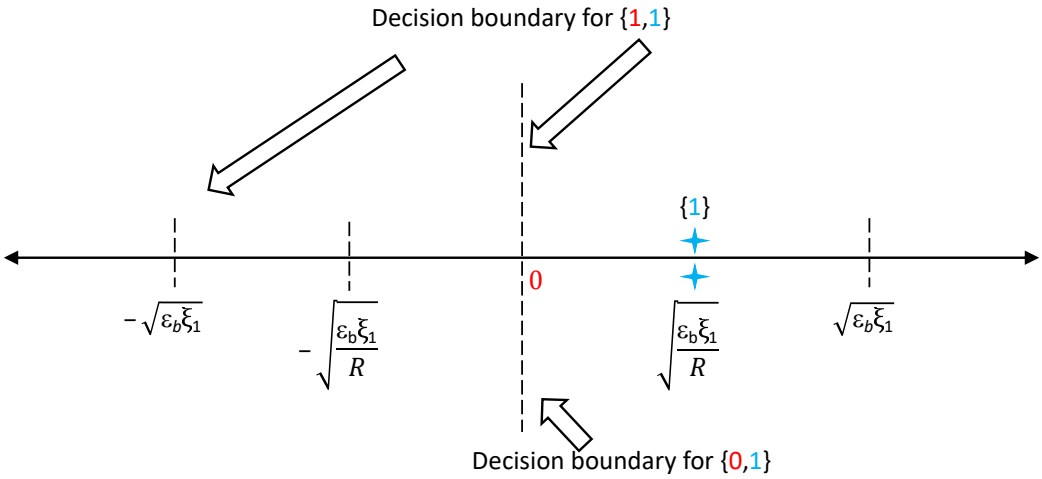

Figure 3.4: Signal space diagram for u_2 with correct u_1 for (0,1) and (1,1)

In the same fashion, it can be found from Fig. 3.4 that the decision boundaries of a_2 decoding for {1,1} in case I are $(-\sqrt{\varepsilon_b\xi_1} - \sqrt{(\varepsilon_b\xi_1)/R})$ and $-\sqrt{(\varepsilon_b\xi_1)/R}$. Similarly, decision boundary of a_2 decoding for {0,1} is $-\sqrt{(\varepsilon_b\xi_1)/R}$ in case I as shown in Fig. 3.4. Therefore, the error probability of a_2 for case I can be expressed as

$$P_{2I}(e) = \frac{1}{4}\left[2\,\mathrm{erfc}\left(\sqrt{\frac{(\varepsilon_b\xi_1)/R}{N_0}}\right) - \mathrm{erfc}\left(\frac{\sqrt{\varepsilon_b\xi_1} + \sqrt{(\varepsilon_b\xi_1)/R}}{\sqrt{N_0}}\right)\right]. \tag{3.4}$$

For case II, Fig. 3.5 describes the signal space diagram of a_2 for {0,0} and {1,0} scenario when u_1 has been incorrectly decoded. The decoding of u_2

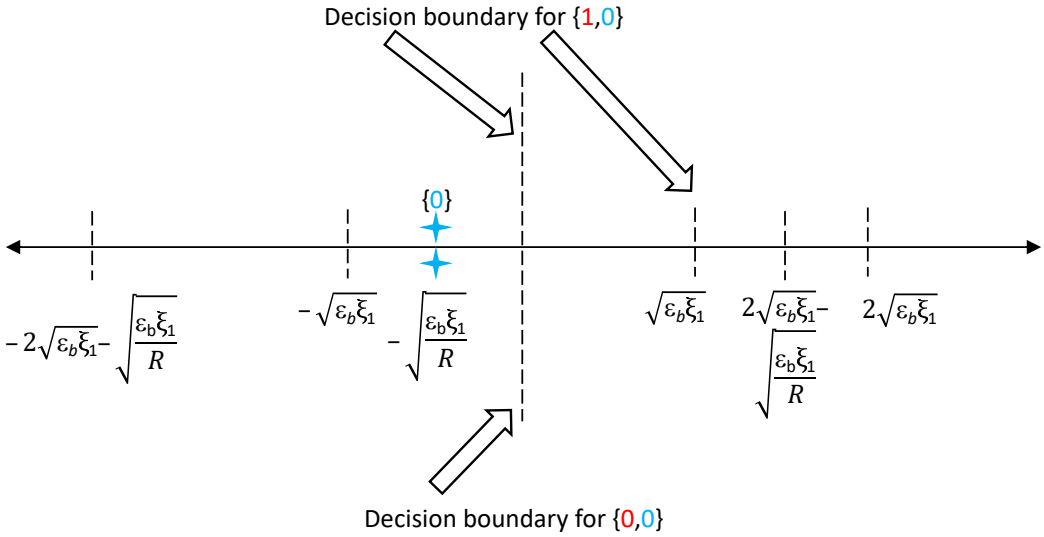

Figure 3.5: Signal space diagram for u_2 with incorrect u_1 for (0,0) and (1,0)

will be affected by the wrong decoding of u_1 because of error propagation during the SIC process. It can be seen in Fig. 3.5 that for {0,0} case, u_2 constellation point is shifted from $-\sqrt{(\varepsilon_b\xi_1)/R}$ to $(-2\sqrt{\varepsilon_b\xi_1}-\sqrt{(\varepsilon_b\xi_1)/R})$. For wrong decoding of a_1, it can be inferred from Fig. 3.2 that noise has to exceed $(\sqrt{\varepsilon_b\xi_1}+\sqrt{(\varepsilon_b\xi_1)/R})$. Moreover, for wrong decoding of a_2, noise has to exceed $(2\sqrt{\varepsilon_b\xi_1}+\sqrt{(\varepsilon_b\xi_1)/R})$ as shown in Fig. 3.5. Therefore, decision boundary for decoding a_2 for {0,0} in case II is $(2\sqrt{\varepsilon_b\xi_1}+\sqrt{(\varepsilon_b\xi_1)/R})$.

For decoding of {1,0} scenario in case II, it can be seen from Fig. 3.5 that the constellation point is shifted from $-\sqrt{(\varepsilon_b\xi_1)/R}$ to $(2\sqrt{\varepsilon_b\xi_1}-\sqrt{(\varepsilon_b\xi_1)/R})$. AWGN should be less than $(-\sqrt{\varepsilon_b\xi_1}+\sqrt{(\varepsilon_b\xi_1)/R})$ for an error in a_1 which will induce a residual error in a_2 decoding. The bit a_2 will be decoded incorrectly if AWGN is more than $(-2\sqrt{\varepsilon_b\xi_1}+\sqrt{(\varepsilon_b\xi_1)/R})$. Therefore the decision boundaries for decoding a_2 for {1,0} scenario in case II are $(-2\sqrt{\varepsilon_b\xi_1}+\sqrt{(\varepsilon_b\xi_1)/R})$ and $(-\sqrt{\varepsilon_b\xi_1}+\sqrt{(\varepsilon_b\xi_1)/R})$.

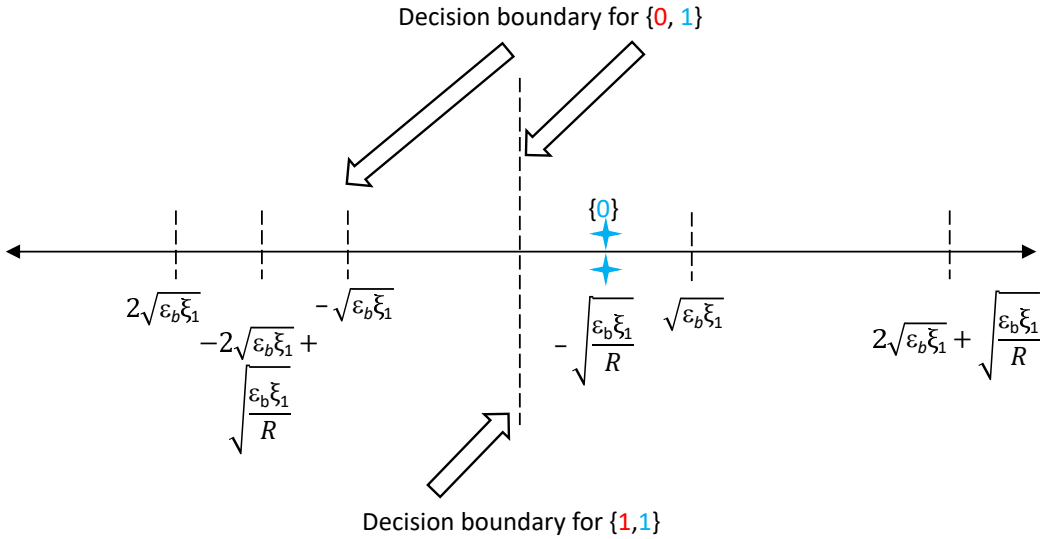

Figure 3.6: Signal space diagram for u_2 with incorrect u_1 for (0,1) and (1,1)

Using the same inference technique in Fig. 3.6, decision boundary for incorrect decoding of user 2 BPSK bit a_2 for {1,1} scenario in case II is $(-2\sqrt{\varepsilon_b\xi_1} - \sqrt{(\varepsilon_b\xi_1)/R})$. Similarly, decision boundaries for {0,1} scenario are $(\sqrt{\varepsilon_b\xi_1} - \sqrt{(\varepsilon_b\xi_1)/R})$ and $(2\sqrt{\varepsilon_b\xi_1} - \sqrt{(\varepsilon_b\xi_1)/R})$ as found from Fig. 3.6. Therefore, the error probability of a_2 for case II can be expressed as

$$\begin{aligned} P_{2II}(e) = &\frac{1}{4}\left[\text{erfc}\left(\frac{2\sqrt{\varepsilon_b\xi_1}+\sqrt{(\varepsilon_b\xi_1)/R}}{\sqrt{N_0}}\right)+\right. \\ &\text{erfc}\left(\frac{\sqrt{\varepsilon_b\xi_1}-\sqrt{(\varepsilon_b\xi_1)/R}}{\sqrt{N_0}}\right)- \\ &\left.\text{erfc}\left(\frac{2\sqrt{\varepsilon_b\xi_1}-\sqrt{(\varepsilon_b\xi_1)/R}}{\sqrt{N_0}}\right)\right], \end{aligned} \tag{3.5}$$

Finally, the exact average BER of u_2 over an AWGN channel can be found as the sum of two different cases given by (3.4) and (3.5) as

$$
\begin{aligned}
P_2(e) =& \frac{1}{4}\left[2\,\mathrm{erfc}\left(\sqrt{\frac{(\varepsilon_b\xi_1)/R}{N_0}}\right) - \right.\\
&\mathrm{erfc}\left(\frac{\sqrt{\varepsilon_b\xi_1}+\sqrt{(\varepsilon_b\xi_1)/R}}{\sqrt{N_0}}\right) + \\
&\mathrm{erfc}\left(\frac{2\sqrt{\varepsilon_b\xi_1}+\sqrt{(\varepsilon_b\xi_1)/R}}{\sqrt{N_0}}\right) + \\
&\mathrm{erfc}\left(\frac{\sqrt{\varepsilon_b\xi_1}-\sqrt{(\varepsilon_b\xi_1)/R}}{\sqrt{N_0}}\right) - \\
&\left.\mathrm{erfc}\left(\frac{2\sqrt{\varepsilon_b\xi_1}-\sqrt{(\varepsilon_b\xi_1)/R}}{\sqrt{N_0}}\right)\right].
\end{aligned}
\tag{3.6}
$$

Chapter 4

Numerical and Simulation Results in AWGN Channel

This chapter presents the numerical results in a single cluster two-user NOMA-BackCom system by evaluating the BER expressions derived in the previous section. The results are validated with Monte Carlo simulations and are found to perfectly match the derived expressions in this paper. Information symbols x_1 and x_2 for both users are selected uniformly from a BPSK constellation and passed through AWGN channels. SIC decoding is implemented at the reader, where, u_2 is decoded after decoding and subtracting reconstructed u_1 symbols from aggregate received signal y.

In Fig. 4.1, numerical and simulated BER of the NOMA enhanced BackCom system is plotted against transmit SNR of both BNs. As can be seen from the figure, numerical results obtained using (5.4) and (3.6) perfectly match the simulation results for different pairs of ξ_1 and ξ_2 values. It can be observed that a greater separation in reflection coefficient values results

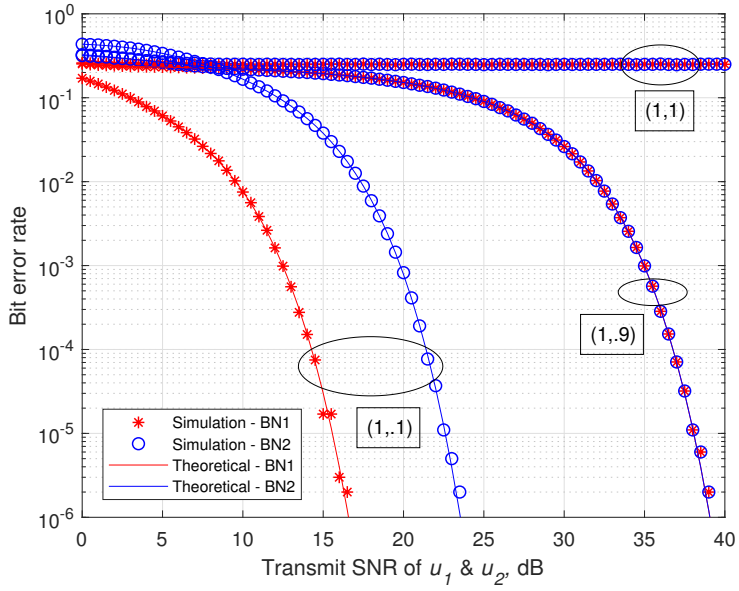

Figure 4.1: BER plots of BN1 and BN2 for three reflection coefficient pairs (ξ_1,ξ_2)

in better BER behavior for NOMA enhanced BackCom. This is because by lowering the BN2 reflection coefficient, ξ_2, the IUI experienced by BN1 is decreased, resulting in better BER performance due to the efficient utilization of the NOMA principle. This effect is highlighted by observing the (1,1) reflection coefficient pair which is essentially a NOMA without the BackCom system and provides unacceptable performance in such a scenario.

Fig. 4.2 illustrates the increase in effective non-erroneous bits transmission by employing the NOMA scheme in a BackCom system with two BNs as compared to an OMA-TDMA transmission scheme. The analysis is carried out over a sufficiently large number of time slots. It can be observed that the NOMA scheme indeed outperforms the OMA scheme due to the simultaneous transmission of two bits to the reader in a single time slot even though

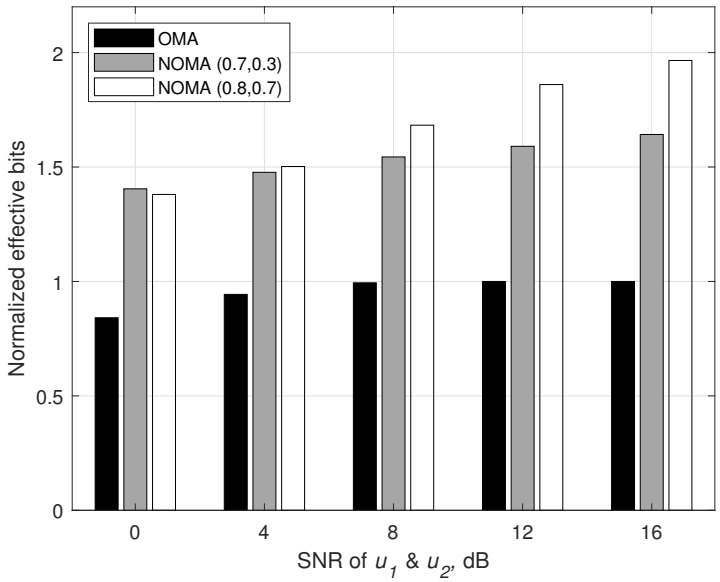

Figure 4.2: Comparison of normalized effective bits transmitted in NOMA for two reflection coefficient pairs (ξ_1,ξ_2) and OMA

the OMA-TDMA scheme experiences no IUI from the second BN. Moreover, the correct transmission of bits is greatly influenced by the reflection coefficients set at the BNs. Reflection coefficients with greater separation result in better performance of the BackCom system.

In the next two simulations, analysis of reflection coefficients will be carried out to find the most optimal reflection coefficient pairs for the NOMA-BackCom system. The simulation parameters are defined in the Table. 4.1.

In Fig. 4.3, contour plot of BER is plotted by varying the two reflection coefficient pairs of BN1 and BN2. Path loss is included in both the forward and backscatter channel. The reflection coefficients of both the BNs are varied from 0.01 to a maximum value of 1 by always keeping ($\xi_1 > \xi_2$) as found from the previous result in Fig. 4.1. BER of BN1 is represented by a

Table 4.1: Simulation parameters.

Parameters	Values
Transmit power of reader P_t	20 dBm
Noise variance N_0	-90 dBm
Path loss exponent α	2
BN1 distance from reader	25 m
BN2 distance from reader	25 m
Effective SNR of BN1 and BN2	24.08 dB

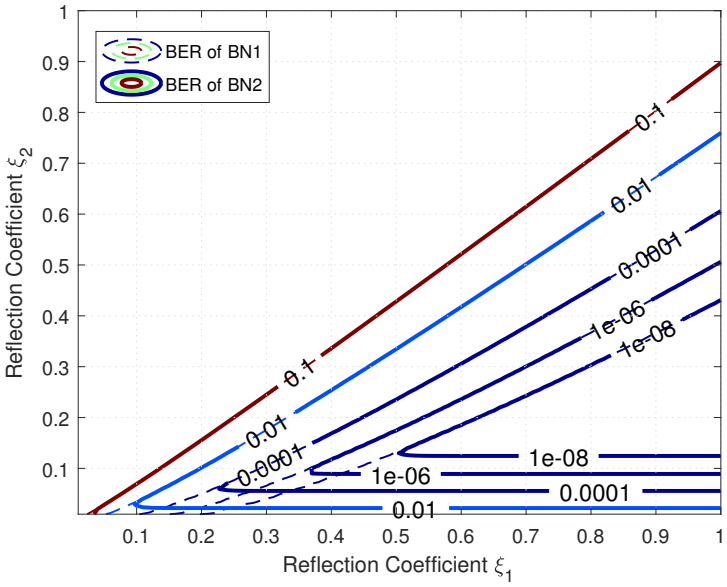

Figure 4.3: BER contour plot by varying ξ_1 and ξ_2 values

dotted line while the BER of BN2 is represented by a solid line. It can be observed from the contour plot that for any specific value of ξ_1, there exists a small range of ξ_2 values smaller than ξ_1 for which we can achieve acceptable performance in a NOMA-BackCom system. This is because by increasing ξ_2, there is an increase in error propagation from BN1 to BN2 which degrades the BER performance. An interesting result of this analysis is that there is

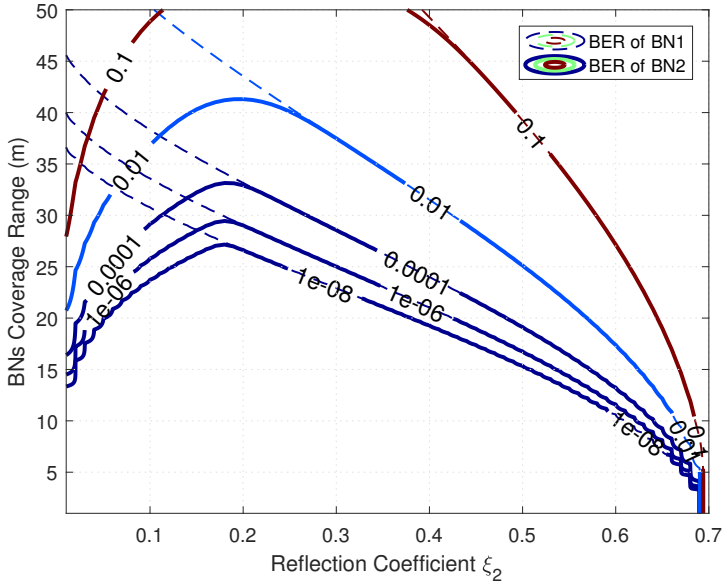

Figure 4.4: BER contour plot of BackCom coverage range versus ξ_2

a limit for the maximum disparity between ξ_1 and ξ_2 values because if ξ_2 value is set too low, the BN2 will not be able to decode itself even with no error propagation from BN1. It should be noted that the BER performance of BN1 is independent of the value of ξ_2.

In Fig. 4.4, analysis of coverage range of the reader is carried out for different values of ξ_2 by setting the reflection coefficient of BN1 (ξ_1) as 0.7. It can be inferred from the figure that for the aforementioned condition, the best coverage is achieved by using ξ_2 which is almost quarter the value of ξ_1, e.g., if the Quality of Service (QoS) requirement of BER for both BN1 and BN2 is 10^{-3}, and the required coverage range for BackCom operation is 33 meters, then the reflection coefficient of BN2 could be set as 0.19 to meet these objectives. The reader's performance starts to fall off by either increase or decrease from this optimum value. Similarly, optimal values of reflection

coefficients for other scenarios may be found.

Chapter 5

NOMA-BackCom Systems in Nakagami-m Channel

5.1 System Model

5.1.1 BackCom Model

We consider a NOMA-aided bistatic BackCom system (BBCS) consisting of a CE, multiple BSNs, and a BSR as shown in Fig. 5.1. In practice, BSNs are usually multiplexed into different clusters of two or three users to maintain low decoding complexity and meet timing constraints. Moreover, CEs are placed closer to the BSNs in the field to mitigate the doubly near-far effect. The BSNs do not possess any active RF transmission source. The CE transmits a sinusoidal continuous wave (CW) carrier signal which is intelligently reflected by BSNs to aid in communication with BSR. The CW signal is transmitted by CEs all the time, whereas BSNs operate in two

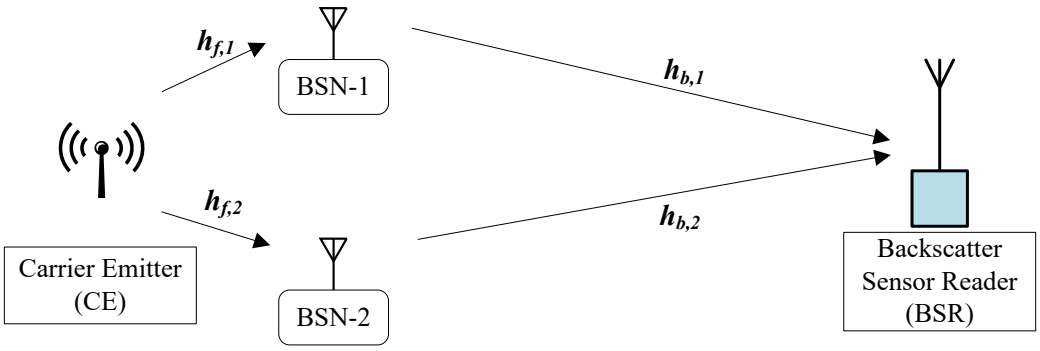

Figure 5.1: Illustration of uplink NOMA-aided BBCS.

states, namely the active state and energy harvesting state.

In the *active state*, each cluster of BSNs backscatters the CW signal to transmit its sensor data to the BSR. The BSR receives the signal and recovers the information from BSNs. BSNs are capable of reflecting the incident CW signal with altered phase and/or magnitude by terminating its antenna between two load impedances. This is typically carried out with the help of an RF transistor. Ideally, by switching the transistor on, the antenna is short-circuited and the incident wave is reflected with a phase change of 180 Alternatively, by switching the transistor off, the antenna is open-circuited and the incident wave is reflected with no phase change (i.e., zero degree). By changing the value of load impedance from short and open-circuit conditions, the magnitude of the reflected wave can also be changed alongside phase.

In the *energy harvesting state*, the BSNs do not reflect the incident CW signal, but only harvest the energy from it. The harvested energy is stored in a battery and is used to power the circuitry (including micro-controller and RF transistor) and support sensing operations. We assume that the cluster

which is not in an active state is in an energy harvesting state or vice versa. Furthermore, the stored energy can be used to sustain long term operations of BSNs.

As the modulation of BSNs is achieved by switching the antenna loads between M load impedances, it corresponds to the power reflection coefficients, Γ_n, $n = \{0, \ldots, M-1\}$. Keeping in view the complexity and energy constraints of the low-power BSNs, we consider BPSK modulation in this work. Therefore, we only consider two values of power reflection coefficient $\{\Gamma_0, \Gamma_1\}$ corresponding to two load impedances. The switching of RF transistor between the two states for the BPSK modulation is performed with the help of a micro-controller. A typical BSN (see Fig. 5.2) circuit consists of an antenna, transmitter, receiver, energy harvester, variable impedances, micro-controller, sensor, RF transistor switch, and a battery.

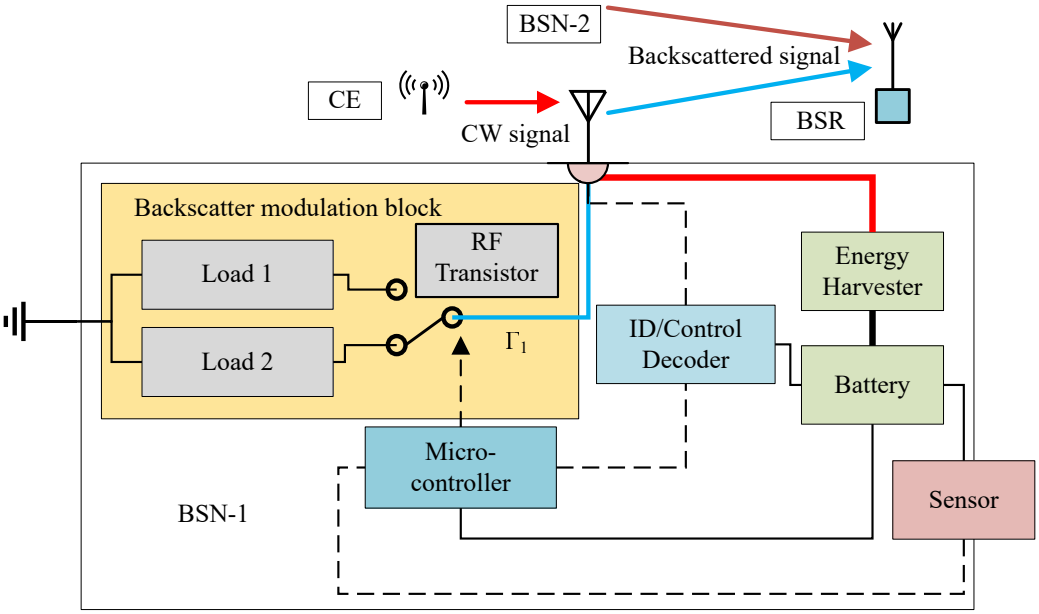

Figure 5.2: Illustration of the internal structure of a BSN.

5.1.2 Channel Model

We consider an uplink transmission scenario in which each cluster of two BSNs is served by a single CE and BSR. Both BSNs and BSRs are equipped with single antennas. As shown in Fig. 5.1, $h_{f,i}$ is used to denote the channel coefficient of the forward link between the CE and ith BSN, for $i \in \{1, 2\}$, whereas $h_{b,i}$ is used to denote the channel coefficient of the backscatter link between ith BSN and BSR.

For the *forward channel*, path loss only propagation effects are considered in $h_{f,i}$. This fading-free channel model is a reasonable channel assumption because of the proximity and strong line-of-sight (LoS) link between CE and BSNs[1]. Combined with our BackCom model and given that the transmit power of the CE is P_T, the power required at a BSN for forward channel is given by $P_T\, \Gamma_i\, |h_{f,i}|^2$. In the *backscatter channel*, we assume that the channel coefficient $h_{b,i}$ follow independent and non-identically distributed (i.n.i.d) Nakagami-m fading which can model both LoS and non-LoS conditions. The zero mean additive white Gaussian noise (AWGN), w, with variance N_0, i.e., $w \sim \mathcal{CN}(0,\, N_0)$ is also considered in the system.

5.1.3 NOMA Scheme

We employ a power-domain NOMA (PD-NOMA) uplink scheme in the BackCom system. PD-NOMA operates by multiplexing users with relatively large channel gain differences over same time/frequency slot, thereby improving spectral efficiency. During IoT deployment, sometimes grouping IoTs with

[1]A fading impaired channel model for forward link is left as a future study at the moment.

nearly balanced power differences is inevitable. However, in IoT scenarios where conventional PD-NOMA is unusable, its BackCom variant can still function by manipulating the power reflection coefficients of the BSNs to generate acceptable channel differences. In a cluster of two BSNs, a training phase is required by the BackCom to differentiate the BSNs into a weak or strong user. It works as follows: each BSN is distinguishable by its unique ID which is known to the BSR. The BSR broadcasts a pilot signal with the unique ID for each BSN in two training time slots. The BSNs backscatter the signal with the same power reflection coefficient after receiving its unique ID. Now, the BSR can obtain the instantaneous channel state information (CSI) and can classify the BSNs into weak/strong pair. The BSNs can then set its power reflection coefficients corresponding to the received instantaneous CSI by the BSR.

For a single cluster, the received signal at the BSR can be written as

$$y = \sqrt{P_T \Gamma_1} h_{f,1} h_{b,1} x_1 + \sqrt{P_T \Gamma_2} h_{f,2} h_{b,2} x_2 + w, \tag{5.1}$$

where x_i is the BPSK modulated information signal of ith nodes. As mentioned earlier, the forward channels $h_{f,i}$s are assumed to be dominated by a deterministic path loss model only, whereby their effects are compensated in the transmit SNR of both BSNs and are thus omitted in further analysis. In order to decode the signals transmitted by the BSNs, successive interference cancellation (SIC) process is implemented at the BSR, where error propagation may happen. Without the loss of generality, it assumed that the first BSN has higher channel gain than the second BSN, i.e., $|h_{b,1}|^2 > |h_{b,2}|^2$. To

detect the weaker signal in a SIC scheme, the stronger signal should be detected first and scaled, then subtracted from the aggregate received signal. Therefore, the optimal decoding order is in the order of decreasing channel gains. Considering this, the signal from BSN-1, u_1, is decoded firstly by treating BSN-2, u_2, as inter-user interference (IUI) at the BSR. Thus the maximum likelihood detector (MLD) of u_1, given that the channel gains are estimated perfectly at BSR, can be described by [46]

$$\widehat{x}_1 = \underset{\widetilde{x}_1 \in \mathcal{S}}{\arg\min} \left| y - \sqrt{P_T \Gamma_1} h_{b,1} \widetilde{x}_1 \right|^2, \tag{5.2}$$

where $\widehat{x}_1$ is the estimated data symbol, $\mathcal{S}$ is the set of all possible constellation points for u_1, and $\widetilde{x}_1$ is the set of all possible trial values for x_1.

Next, u_2 signal is decoded after subtracting the detected u_1 symbol from received composite signal y. If u_1's signal is decoded correctly then no IUI is faced in decoding of u_2, otherwise, there will be error propagation from u_1 while decoding u_2. The detector for u_2 can be expressed as

$$\widehat{x}_2 = \underset{\widetilde{x}_2 \in \mathcal{S}}{\arg\min} \left| \left(y - \sqrt{P_T \Gamma_1} h_{b,1} \widehat{x}_1 \right) - \sqrt{P_T \Gamma_2} h_{b,2} \widetilde{x}_2 \right|^2. \tag{5.3}$$

In the next section, BER expressions are derived for PD-NOMA-BackCom system with a cluster of two BSNs, assuming equiprobable symbols. The same approach may be applied for a higher order phase shift keying (PSK) modulation, however, the derivation becomes impractical when a large number of BSNs are multiplexed together.

5.2 NOMA-BackCom BER Performance Analysis

As noted from (5.1), the received symbol at BSR is a superposition of two BPSK symbols, therefore, it corresponds to a total of four constellation points as shown in Fig. 5.3. Because $|h_{b,1}|^2 > |h_{b,2}|^2$, the BSR detects u_1 symbol first. Thereafter, it subtracts the decoded u_1 symbol from the received signal and detects u_2 symbol. Each constellation point in Fig. 5.3 is represented by two bits given by $\{x_1, x_2\}$. Here, x_1 is the BPSK bit of u_1 and x_2 is the BPSK bit of u_2. In Fig. 5.3, red diamond shows the original location of x_1 without IUI from u_2. However, because of the presence of IUI from u_2, x_1 is translated to two possible constellation points. The shaded block shows the two possible values that a particular u_1 bit x_1 may take due to IUI. By modifying the values of reflection coefficients, the position of these constellation points can be changed, which will in turn affect the BER performance of the system.

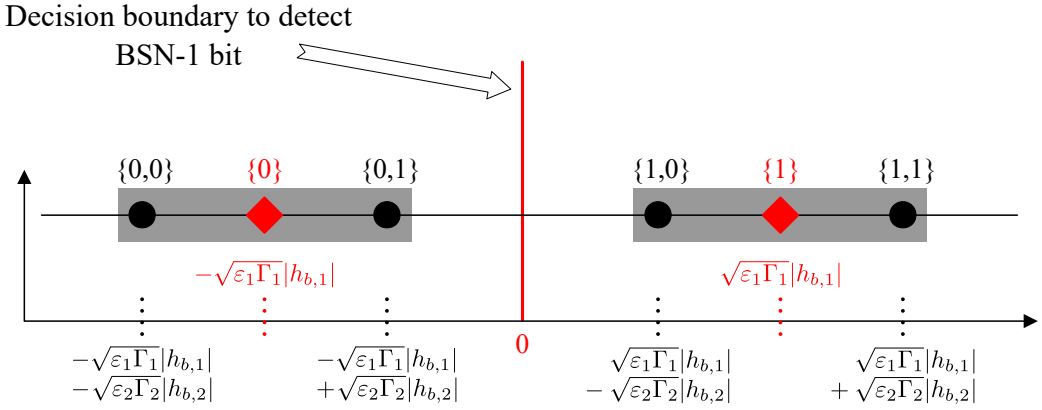

Figure 5.3: The received signal space diagram of super-imposed BPSK symbols from two BSNs at the BSR, where $|h_{b,1}|^2 > |h_{b,2}|^2$.

5.2.1 BER of the First User

The detection of the first user is performed according to (5.2), therefore, no SIC is required in the process. An error will be made in the detection process if $\widehat{x}_1 \neq x_1$ and its probability is given by $P_e(u_1)$. The probability of error for u_1 depends on the decision boundary distance of x_1 and it is the sum of error probabilities of each possible symbol multiplied with the prior probability. Because of IUI, there are four possible cases in which a bit x_1 can be decoded incorrectly. When $u_1^{(0)}$ and $u_2^{(0)}$ are sent, where $u_i^{(y)}$ represents that user i transmits a bit y, the decision boundary of x_1, represented by the red line, is at a distance of $\sqrt{\varepsilon_1\Gamma_1}|h_{b,1}| + \sqrt{\varepsilon_2\Gamma_2}|h_{b,2}|$ from the constellation point $\{0, 0\}$, where ε_i denote the symbol energy of user i. Therefore, bit x_1 will be decoded incorrectly if in-phase component of w exceeds the sum of $u_1^{(0)}$ and $u_2^{(0)}$ i.e., $w \geq \sqrt{\varepsilon_1\Gamma_1}|h_{b,1}| + \sqrt{\varepsilon_2\Gamma_2}|h_{b,2}|$. Similarly, following the same procedure for each symbol, the error is calculated and multiplied by prior probability. Consequently, the error probability for u_1, considering even symmetry in constellation diagram, is given by

$$P_e(u_1) = \frac{1}{4}\left[\mathbb{P}(|w| \geq \Upsilon_1 + \Upsilon_2) + \mathbb{P}(|w| \geq \Upsilon_1 - \Upsilon_2)\right], \tag{5.4}$$

where $\mathbb{P}(x)$ denotes the probability of event x, and $\Upsilon_i = \sqrt{\varepsilon_i\Gamma_i}|h_{b,i}|$. The expression (5.4) can be represented using Gaussian $\mathcal{Q}$ function as

$$P_e(u_1) = \frac{1}{2}\left[\mathcal{Q}\left(Y\right) + \mathcal{Q}\left(Z\right)\right], \tag{5.5}$$

where Y and Z are random variables (RVs), defined as

$$\begin{aligned} Y &= \frac{\Upsilon_1}{\sqrt{N_0/2}} + \frac{\Upsilon_2}{\sqrt{N_0/2}}, \\ Z &= \frac{\Upsilon_1}{\sqrt{N_0/2}} - \frac{\Upsilon_2}{\sqrt{N_0/2}}, \end{aligned} \tag{5.6}$$

and the Gaussian $\mathcal{Q}$ function is defined as

$$\mathcal{Q}(x) = \frac{1}{2\pi} \int_x^\infty \exp\left(-\frac{u^2}{2}\right) \mathrm{d}u. \tag{5.7}$$

The average BER for BSN-1, denoted as $\overline{P_e(u_1)}$, is evaluated by averaging over the PDF of RV Y, $f_Y(y)$, and RV Z, $f_Z(z)$, where, $f_Y(y)$ and $f_Z(z)$ are the PDFs for the sum and difference of two i.n.i.d Nakagami-m distributions, respectively. The average error probability of u_1 is

$$\overline{P_e(u_1)} = \frac{1}{2}\left[\int_{-\infty}^{\infty} \mathcal{Q}\left(Y\right) f_Y(y)\, \mathrm{d}y + \int_{-\infty}^{\infty} \mathcal{Q}\left(Z\right) f_Z(z)\, \mathrm{d}z\right]. \tag{5.8}$$

The PDF $f_Y(y)$ has been derived in [47] and [48] in the form of Appell hypergeometric function of the second kind and Lauricella multivariable hypergeometric function, respectively. However, a closed-form solution of (5.8) is prohibited using expressions in [47] and [48], rendering the use of numerical evaluation. Therefore, the PDF of Y in this work is approximated with another distribution, complying with the features of Y as shown in the following lemma.

Lemma 1: The distribution of the sum of two i.n.i.d Nakagami-m_i RVs, Y_1 and Y_2, with parameters m_i and Ω_i, where $i \in \{1, 2\}$, can be approximated

by another Nakagami-m_{R_1} RV R_1, i.e., $R_1 = Y_1 + Y_2$, with fading parameter m_{R_1} and average power Ω_{R_1}, with PDF as

$$f_{R_1}(r) = \frac{2m_{R_1}^{m_{R_1}} r^{2m_{R_1}-1}}{\Omega_{R_1}^{m_{R_1}} \Gamma(m_{R_1})} \exp(-\frac{m_{R_1} r^2}{\Omega_{R_1}}), \quad r_1 > 0, \tag{5.9}$$

where Ω_{R_1} and m_{R_1} are defined as [49]

$$\begin{aligned} \Omega_{R_1} &= \mathbb{E}[{R_1}^2], \\ m_{R_1} &= \frac{(\mathbb{E}[{R_1}^2])^2}{Var[{R_1}^2]} = \frac{\Omega_{R_1}^2}{\mathbb{E}[{R_1}^4] - \Omega_{R_1}^2}, \end{aligned} \tag{5.10}$$

where $\Gamma(.)$ is the gamma function, and $\mathbb{E}[.]$ and $Var[.]$ denote the expectation and variance operators, respectively.

Proof: A two-step process is followed to approximate the distribution of the sum of two RVs Y_1 and Y_2 to another distribution. In the first step, the method of moments (MoM) approach is utilized to match the moments of RV $Y = Y_1 + Y_2$ to that of Nakagami-m_{R_1} RV, R_1. Nakagami-m distribution is based on two parameters, i.e., fading parameter m and shape parameter Ω. Therefore, we need to match the moments of the two parameters. From [49], the nth moment of the Nakagami-m_i distribution is given by

$$\mathbb{E}[Y_i^n] = \frac{\Gamma(m_i + \frac{n}{2})}{\Gamma(m_i)} \left(\frac{\Omega_i}{m_i}\right)^{\frac{n}{2}}, \tag{5.11}$$

where m_i is the fading parameter of each RV Y_i, $\Omega_1 = \Omega_{Y_1} = 2\Upsilon_1^2/N_0$ and $\Omega_2 = \Omega_{Y_2} = 2\Upsilon_2^2/N_0$. Using the multinomial theorem assuming independence among RVs, Y_1, Y_2, and (5.11), the second moment of the sum RV $Y = Y_1 + Y_2$

is matched with the second moment of RV R_1, i.e.,

$$\begin{aligned}\Omega_{R_1} &= \mathbb{E}[Y^2] = \mathbb{E}[Y_1^2] + \mathbb{E}[Y_2^2] + 2\mathbb{E}[Y_1]\mathbb{E}[Y_2] \\ &= \Omega_1 + \Omega_2 + 2\frac{\Gamma(m_1+\frac{1}{2})}{\Gamma(m_1)}\left(\frac{\Omega_1}{m_1}\right)^{\frac{1}{2}}\frac{\Gamma(m_2+\frac{1}{2})}{\Gamma(m_2)}\left(\frac{\Omega_2}{m_2}\right)^{\frac{1}{2}}. \end{aligned} \tag{5.12}$$

Now we need to find the value of m_{R_1}. To this objective, we note from (5.10) that $\mathbb{E}[{R_1}^4]$ is required. Again using the multinomial theorem for $R_1 = Y_1 + Y_2$, $\mathbb{E}[{R_1}^4]$ can be evaluated as

$$\mathbb{E}[{R_1}^4] = \mathbb{E}[Y_1^4] + 4\mathbb{E}[Y_1^3]\mathbb{E}[Y_2] + 6\mathbb{E}[Y_1^2]\mathbb{E}[Y_2^2] + 4\mathbb{E}[Y_1]\mathbb{E}[Y_2^3] + \mathbb{E}[Y_2^4]. \tag{5.13}$$

Then, from (5.10) and (5.12), value of m_{R_1} can easily be found.

In the second step, the Kolmogorov-Smirnov (K-S) test is used for goodness-of-fit (see Appendix). Fig. 5.4(a) shows the plot of empirical CDF and approximated theoretical CDF [50].

The PDF $f_Z(z)$ for the difference of two i.n.i.d Nakagami-m distributions has not been derived previously. Therefore, we approximate it with another closely matching distribution using the following lemma.

Lemma 2: The distribution of the difference of two i.n.i.d Nakagami-m_i RVs, Z_1 and Z_2, with parameters m_i and Ω_i, where $i \in \{1, 2\}$, can be approximated by a Gaussian (normal) RV, $W_1 = Z_1 - Z_2$, with mean μ_{W_1} and variance $\sigma_{W_1}^2$, with PDF

$$f_{W_1}(w) = \frac{1}{\sqrt{2\pi\sigma_{W_1}^2}} \exp\left(-\frac{(w-\mu_{W_1})^2}{2\sigma_{W_1}^2}\right), \tag{5.14}$$

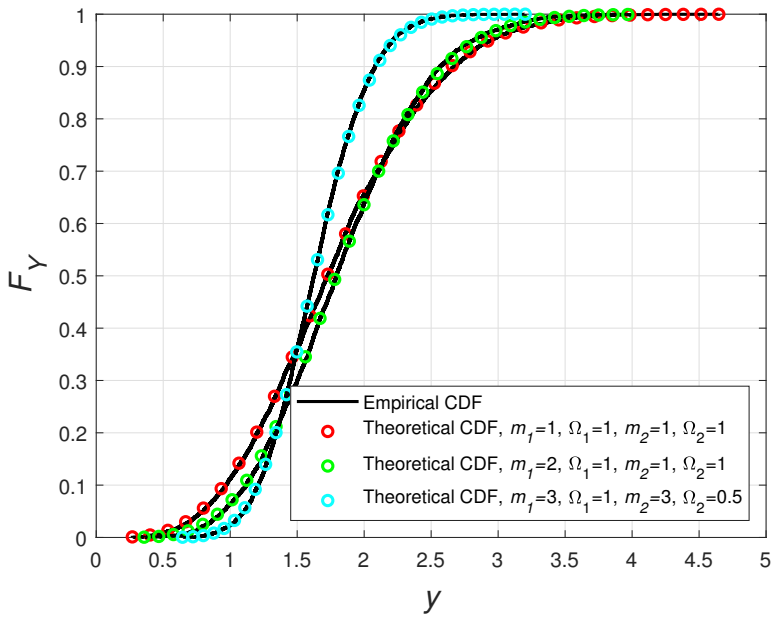

(a)

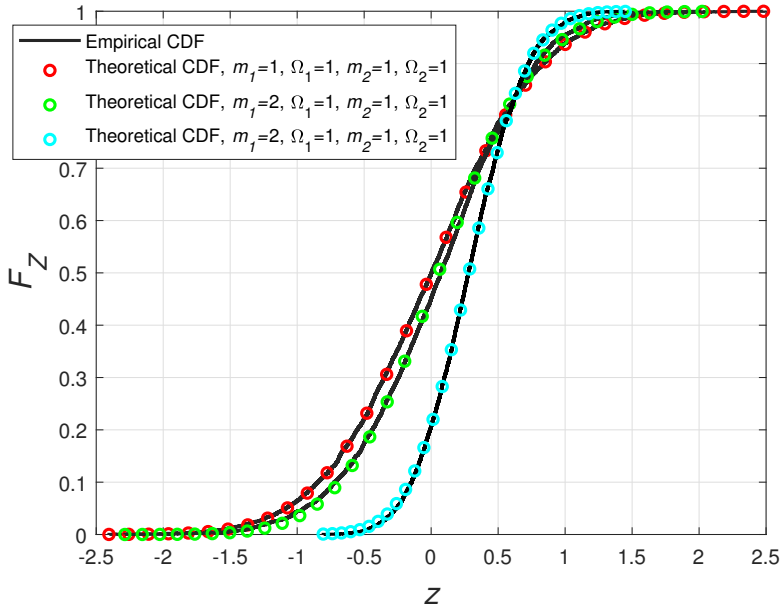

(b)

Figure 5.4: Empirical CDF vs theoretical CDF obtained using MOM with two i.n.i.d Nakagami-m distributions; (a) the sum of the two, (b) the difference of two.

where the values of μ_{W_1} and $\sigma^2_{W_1}$ are given in (5.16) and (5.17).

Proof: A similar two-step process as used in Lemma 1, is used to approximate the distribution of the difference of two RVs Z_1 and Z_2 to another distribution. Firstly, MoM is applied to match the moments of RV $Z = Z_1 - Z_2$ to moments of the normal RV, W_1. The first two moments of W_1 are

$$\begin{aligned} \mathbb{E}[W_1] &= \mu_{W_1}, \\ \mathbb{E}[{W_1}^2] &= \mu^2_{W_1} + \sigma^2_{W_1}. \end{aligned} \tag{5.15}$$

Following the algorithm of moment matching, using multinomial theorem, noting independence among RVs, Z_1 and Z_2, and using (5.11), the mean μ_{W_1} of the normal RV, W_1, can be evaluated by matching the first moment of the difference RV $Z = Z_1 - Z_2$ with RV W_1 as

$$\begin{aligned} \mu_{W_1} &= \mathbb{E}[Z] = \mathbb{E}[Z_1] - \mathbb{E}[Z_2] \\ &= \frac{\Gamma(m_1 + \frac{1}{2})}{\Gamma(m_1)} \left(\frac{\Omega_1}{m_1}\right)^{\frac{1}{2}} - \frac{\Gamma(m_2 + \frac{1}{2})}{\Gamma(m_2)} \left(\frac{\Omega_2}{m_2}\right)^{\frac{1}{2}}, \end{aligned} \tag{5.16}$$

where $\Omega_1 = \Omega_{Z_1} = 2\Upsilon_1^2/N_0$ and $\Omega_2 = \Omega_{Z_2} = 2\Upsilon_2^2/N_0$. Now we match the second moments to obtain variance $\sigma^2_{W_1}$

$$\begin{aligned} \mu^2_{W_1} + \sigma^2_{W_1} &= \mathbb{E}[Z^2] = \mathbb{E}[Z_1^2] + \mathbb{E}[Z_2^2] - 2\mathbb{E}[Z_1]\mathbb{E}[Z_2], \\ \sigma^2_{W_1} &= \mathbb{E}[Z^2] - \mu^2_{W_1}, \end{aligned} \tag{5.17}$$

where $\mathbb{E}[Z_i^n]$ is taken from (5.11).

In the second step, the Kolmogorov-Smirnov (K-S) test is used to show that the normal distribution closely matches the distribution of the difference

of two Nakagami-m RVs. The K-S test is has been performed in Appendix. Fig. 5.4(b) shows the plot of empirical CDF and approximated theoretical CDF showing a close agreement.

Now from (5.9) and (5.14), a closed-form solution for the average BER can be evaluated as follows

$$\overline{P_e(u_1)} = \frac{1}{2}\Big[\underbrace{\int_{-\infty}^{\infty}\mathcal{Q}(R)f_R(r)\,\mathrm{d}r}_{\Phi} + \underbrace{\int_{-\infty}^{\infty}\mathcal{Q}\left(W\right)f_W(w)\,\mathrm{d}w}_{\Lambda}\Big]. \tag{5.18}$$

The closed-form expression for Φ can be found by invoking the alternative form of the Q-function known as Craig's formula [51] and applying moment generating function (MGF) for $f_{\gamma_R}(\gamma_r)$. It is given by

$$\Phi(m,\overline{\gamma}) = \begin{cases} \frac{1}{2}\left[1-\Psi\left(\frac{\overline{\gamma}}{2m}\right)\sum_{k=0}^{m-1}\left(\frac{1-\Psi^2\left(\frac{\overline{\gamma}}{2m}\right)^k}{4}\right)\right], m \text{ integer} \\ \frac{1}{2\sqrt{\pi}}\frac{\sqrt{\frac{\overline{\gamma}}{2m}}}{(1+\frac{\overline{\gamma}}{2m})^{m+(1/2)}}\frac{\Gamma(m+\frac{1}{2})}{\Gamma(m+1)}\times \\ {}_2F_1\left(1, m+\frac{1}{2}; m+1; \frac{m}{m+\frac{\overline{\gamma}}{2m}}\right),\ m \text{ noninteger} \end{cases} \tag{5.19}$$

where $\Psi\left(\frac{\overline{\gamma}}{2m}\right) \triangleq \sqrt{\frac{\overline{\gamma}/2}{m+\overline{\gamma}/2}}$ and ${}_2F_1$ is the Gauss hypergeometric function. Further, the closed-form expression for Λ in (5.18) is given by following Lemma.

Lemma 3: The integral of the product of a Q function and a normal distribution with mean μ and variance σ^2 is

$$\Lambda(\mu,\sigma^2) = \mathcal{Q}\left(\frac{\mu}{\sqrt{\sigma^2+1}}\right). \tag{5.20}$$

Proof: See Appendix.

Finally by using (5.19) and (5.20) in (5.18), the average probability of error for BSN-1 can be expressed as

$$\overline{P_{(e)}(u_1)} = \frac{1}{2}\left[\Phi(m_{R_1}, \Omega_{R_1}) + \Lambda(\mu_{W_1}, \sigma^2_{W_1})\right]. \tag{5.21}$$

5.2.2 BER of the Second User

To decode the second user, SIC process is implemented, whereby, BSR would initially detect the first user according to (5.2) and then from the reconstructed $\widehat{x}_1$ bit, compute,

$$\widehat{x}_2 = \arg\min_{\widetilde{x}_2 \in \mathcal{S}} \left| y_{SIC} + w - \sqrt{P_T \Gamma_2} h_{b,2} \widetilde{x}_2 \right|^2. \tag{5.22}$$

Therefore, if $\widehat{x}_1$ is detected correctly, i.e., $\widehat{x}_1 = x_1$, then $y_{SIC} = \sqrt{P_T \Gamma_2} h_{b,2} x_2$ and it corresponds to an IUI-free decoding. On the other hand, if $\widehat{x}_1$ is detected incorrectly, i.e., $\widehat{x}_1 \neq x_1$, then $y_{SIC} = \sqrt{P_T \Gamma_1} h_{b,1} x_1 + \sqrt{P_T \Gamma_2} h_{b,2} x_2 - \sqrt{P_T \Gamma_1} h_{b,1} \widehat{x}_1$ and the decoding decision for second user also depends on the value of reconstructed bit $\widehat{x}_1$. Fig. 5.5 shows the received signal diagram for the two aforementioned cases when the transmitted u_1 bit $x_1^{(1)}$ is decoded correctly or incorrectly. Therefore, these two cases should be handled differently.

Case I

We first consider the case that u_1 symbol has been detected correctly by BSR. The probability for correct decoding of x_1 bit is opposite to the one derived in (5.4), which gives the probability for incorrect decoding of x_1 bit.

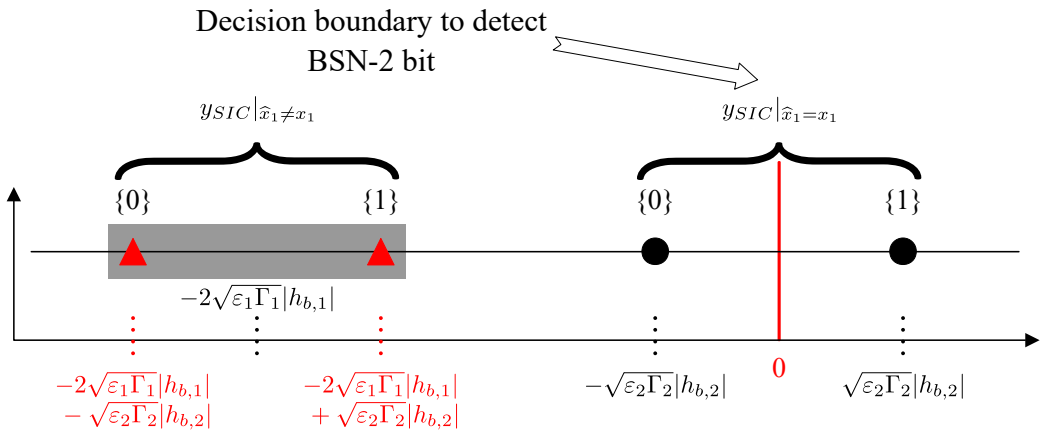

Figure 5.5: The received signal space diagram of BSN-2 for $x_1^{(1)}$ transmission when $y_{SIC}|_{\hat{x}_1 \neq x_1}$ and $y_{SIC}|_{\hat{x}_1 = x_1}$.

$$P_e^I(u_2) = \frac{1}{2}\Big[\mathbb{P}(w \leq \Upsilon_1 + \Upsilon_2) \times \mathbb{P}\big(w \geq \Upsilon_2 \;\big|\; w \leq \Upsilon_1 + \Upsilon_2\big) + \mathbb{P}(w \leq \Upsilon_1 - \Upsilon_2) \times \mathbb{P}\big(w \leq -\Upsilon_2 \;\big|\; w \leq \Upsilon_1 - \Upsilon_2\big)\Big]. \quad (5.23)$$

$$P_e^{II}(u_2) = \frac{1}{2}\Big[\mathbb{P}(w \geq \Upsilon_1 + \Upsilon_2) \times \mathbb{P}\big(w \geq 2\Upsilon_1 + \Upsilon_2 \;\big|\; w \geq \Upsilon_1 + \Upsilon_2\big) + \mathbb{P}(w \geq \Upsilon_1 - \Upsilon_2) \times \mathbb{P}\big(w \leq 2\Upsilon_1 - \Upsilon_2 \;\big|\; w \geq \Upsilon_1 - \Upsilon_2\big)\Big]. \quad (5.24)$$

This will serve as the prior probability for case I. The error probability for x_2 bit is influenced by the decision boundary for detecting u_2 symbol as shown by the constellation points indicated by the black circles in Fig. 5.5. Hence, the probability of error for u_2 with correct u_1 decoding, considering both $x_1^{(0)}$ and $x_1^{(1)}$ bit transmission scenarios, is given by (5.23) at the top of page.

The conditional expressions pertain to decoding the x_1 bit correctly and can be inferred from Fig. 3.2. The first and second terms in (5.23) correspond to $x_2^{(0)}$ and $x_2^{(1)}$ received constellation points, respectively.

Using conditional probability law, (5.23) can be rewritten as

$$P_e^I(u_2) = \frac{1}{2}\left[\mathbb{P}(\Upsilon_2 \leq w \leq \Upsilon_1 + \Upsilon_2) + \mathbb{P}(\Upsilon_2 \leq w)\right]. \tag{5.25}$$

The expression in (5.25) can be represented using Gaussian $\mathcal{Q}$ function as

$$P_e^I(u_2) = \mathcal{Q}(\sqrt{\gamma_{\Upsilon_2}}) - \frac{1}{2}\mathcal{Q}(Y), \tag{5.26}$$

where Y is defined in (5.6) and $\gamma_{\Upsilon_2} = \frac{\Upsilon_2^2}{N_0/2}$.

Case II

This case considers the scenario when u_1 symbol has been detected incorrectly by BSR. The probability for incorrect decoding of x_1 bit is similar to the one derived in (5.4). This will serve as the prior probability for case II. Because of the IUI from u_1, there will be an error propagation of $2\Upsilon_1$ from the decision boundary to detect x_2. This can be observed from the constellation points represented by the red triangles in Fig. 5.5. Hence, the probability of error for u_2 with incorrect u_1 decoding, considering both $x_1^{(0)}$ and $x_1^{(1)}$ bit transmission scenarios, is (5.24).

The conditional expressions in (5.24) are obtained in the same way as in (5.23) except that x_1 is decoded incorrectly in case II. By using conditional probability law, the probability of error for u_2 considering x_1 is decoded erroneously, represented using the Gaussian $\mathcal{Q}$ function, is given by

$$P_e^{II}(u_2) = \frac{1}{2}\left[\mathcal{Q}(C) + \mathcal{Q}(Z) - \mathcal{Q}(D)\right]. \tag{5.27}$$

where Z is defined in (5.6), C and D are RVs, defined as

$$\begin{aligned} C &= \frac{2\Upsilon_1}{\sqrt{N_0/2}} + \frac{\Upsilon_2}{\sqrt{N_0/2}}, \\ D &= \frac{2\Upsilon_1}{\sqrt{N_0/2}} - \frac{\Upsilon_2}{\sqrt{N_0/2}}. \end{aligned} \tag{5.28}$$

Then, the total probability of error for u_2 can be found as the sum of both the cases given by (5.26) and (5.27)

$$\begin{aligned} P_e(u_2) &= P_e^I(u_2) + P_e^{II}(u_2), \\ P_e(u_2) &= \mathcal{Q}(\sqrt{\gamma_{\Upsilon_2}}) + \frac{1}{2}\left[-\mathcal{Q}(Y) + \mathcal{Q}(C) + \mathcal{Q}(Z) - \mathcal{Q}(D)\right]. \end{aligned}$$

The RV C, i.e., sum of two i.n.i.d Nakagami-m_i RVs, can be approximated by a Nakagami-m_{R_2} RV with fading parameter m_{R_2} and average power Ω_{R_2}, with PDF given in (5.9) as proved in Lemma 2, where $\Omega_{C_1} = 4\Omega_1$ and $\Omega_{C_2} = \Omega_2$. The RV D, i.e., difference of two i.n.i.d Nakagami-m_i RVs, can be approximated by a Gaussian (normal) RV, with mean μ_{W_2} and variance $\sigma^2_{W_2}$, with PDF given in (5.14) as proved in Lemma 2, where $\Omega_{D_1} = 4\Omega_1$ and $\Omega_{D_2} = \Omega_2$.

Therefore, the average probability of error for u_2 becomes

$$\begin{aligned} \overline{P_e(u_2)} = \Phi(m_2, \gamma_{\Upsilon_2}) + \frac{1}{2}\big[&-\Phi(m_{R_1}, \Omega_{R_1}) + \Phi(m_{R_2}, \Omega_{R_2}) + \Lambda(\mu_{W_1}, \sigma^2_{W_1}) \\ &-\Lambda(\mu_{W_2}, \sigma^2_{W_2})\big]. \end{aligned} \tag{5.29}$$

5.3 Appendices

5.3.1 K-S Test for the sum of two i.n.i.d Nakagami-m_i RVs

The random number generation routine is repeated N times to collect samples of the RV Y, i.e., $\{y_1, y_2, ..., y_N\}$, with empirical cumulative distribution function (CDF) $\widehat{F}_Y$. The hypothesized CDF is that of Nakagami-m_{R_1} distribution, F_{R_1}. The statistic used for goodness-of-fit known as K-S statistic is the maximum difference between the empirical CDF and hypothesized CDF, given by [52]

$$\widehat{D}_f = \sup_y |\widehat{F}_Y(y_i) - F_{R_1}(y_i)|. \tag{5.30}$$

The critical value is found to be $\widehat{c} = 0.0192$ for $N = 5000$ samples against the level of significance $\widehat{a} = 0.05$. The null hypothesis for testing is given as

$$H_0 : F_Y = F_{R_1}. \tag{5.31}$$

The null hypothesis is accepted if $\widehat{D}_f \leq \widehat{c}$, i.e., $F_Y = F_{R_1}$ and rejected otherwise. The K-S test is conducted for three set of parameters, i.e., $\{m_1 = 1, \Omega_1 = 1, m_2 = 1, \Omega_2 = 1\}$, $\{m_1 = 3, \Omega_1 = 1, m_2 = 1, \Omega_2 = 1\}$ and $\{m_1 = 3, \Omega_1 = 1, m_2 = 3, \Omega_2 = 0.5\}$ and K-S statistic, $\widehat{D}_f$, calculated using (5.30)

are

$$\begin{aligned}
&\widehat{D}_f = 0.0122 \text{ for } m_1 = 1, \Omega_1 = 1, m_2 = 1, \Omega_2 = 1, \\
&\widehat{D}_f = 0.0082 \text{ for } m_1 = 2, \Omega_1 = 1, m_2 = 1, \Omega_2 = 1, \\
&\widehat{D}_f = 0.0077 \text{ for } m_1 = 3, \Omega_1 = 1, m_2 = 3, \Omega_2 = 0.5.
\end{aligned} \tag{5.32}$$

It can be observed, that $\widehat{D}_f \leq \widehat{c}$ for each parameter set and H_0 cannot be rejected. Hence, Nakagami-m distribution closely matches the distribution of the sum of two Nakagami-m RVs and can be used to approximate RV Y.

5.3.2 K-S Test for the difference of two i.n.i.d Nakagami-m_i RVs

Again, the Random number generation routine is repeated N times to collect samples of the RV Z , i.e., $\{z_1, z_2, ..., z_N\}$, with empirical cumulative distribution function (CDF) $\widehat{F}_Z$. The hypothesized CDF is that of normal distribution, F_{W_1}.

The critical value is found to be $\widehat{c} = 0.0192$ for $N = 5000$ samples against the level of significance $\widehat{a} = 0.05$. The null hypothesis for testing is given as

$$H_0 : F_Z = F_{W_1}. \tag{5.33}$$

The K-S test is conducted for three set of parameters, i.e., $\{m_1 = 1, \Omega_1 = 1, m_2 = 1, \Omega_2 = 1\}$, $\{m_1 = 3, \Omega_1 = 1, m_2 = 1, \Omega_2 = 1\}$ and $\{m_1 = 3, \Omega_1 = 1, m_2 = 3, \Omega_2 = 0.5\}$ and K-S statistic, $\widehat{D}_f$, calculated using (5.30) for each set, given as

$$\begin{aligned}
&\widehat{D}_f = 0.0109 \text{ for } m_1 = 1, \Omega_1 = 1, m_2 = 1, \Omega_2 = 1, \\
&\widehat{D}_f = 0.0141 \text{ for } m_1 = 2, \Omega_1 = 1, m_2 = 1, \Omega_2 = 1, \\
&\widehat{D}_f = 0.0140 \text{ for } m_1 = 3, \Omega_1 = 1, m_2 = 3, \Omega_2 = 0.5.
\end{aligned} \tag{5.34}$$

H_0 cannot be rejected for each parameter set as $\widehat{D}_f \leq \widehat{c}$. Hence, normal distribution closely matches the distribution of the difference of two Nakagami-m RV and can be used to approximate RV Z.

5.3.3 Proof of Lemma 2

Let W be a normal distributed RV with parameters mean μ and variance σ^2, i.e., $W \sim N(\mu, \sigma^2)$ and Z be a standard normal distributed RV, i.e., $Z \sim N(0, 1)$. Both being independent, then $\mathcal{Q}(w) = \mathbb{P}(Z > w)$ as $\mathcal{Q}(x)$ is the probability that a standard normal RV takes a value greater than x. This is similar to Λ because the integrand in Λ is the product of $\mathbb{P}(Z > w) = \mathbb{P}(Z > W|W = w)$ and the marginal density of normal RV, W, i.e., $f_W(w)$, which comes out to be $\mathbb{P}(Z > W)$. As we know that distribution of the difference of two normal RVs is again a normal RV with subtracted means but added variances, i.e., $Z - W \sim N(-\mu, \sigma^2 + 1)$, therefore

$$\Lambda = \mathbb{P}(Z > W) = \mathbb{P}(Z - W > 0) = \mathcal{Q}\left(\frac{\mu}{\sigma^2 + 1}\right). \tag{5.35}$$

Chapter 6

Numerical Results and Simulations in Nakagami-m Channel

This section investigates the performance of NOMA enhanced bistatic Back-Com system consisting of a single cluster of two-BSNs and presents the numerical results by evaluating the BER expressions derived in the previous section. The results are validated with Monte Carlo simulations and are found to match the derived expressions in this paper. The channel between BSNs and BSR is modeled as Nakagami-m fading channel, and both BSN and BSR are assumed to be equipped with a single antenna. The transmitted symbols for both users are selected uniformly from a BPSK constellation. Unless stated otherwise, the figures are plotted for fading channel conditions given as $m_1 = 4, \Omega_1 = 1, m_2 = 1, \Omega_2 = 0.5$.

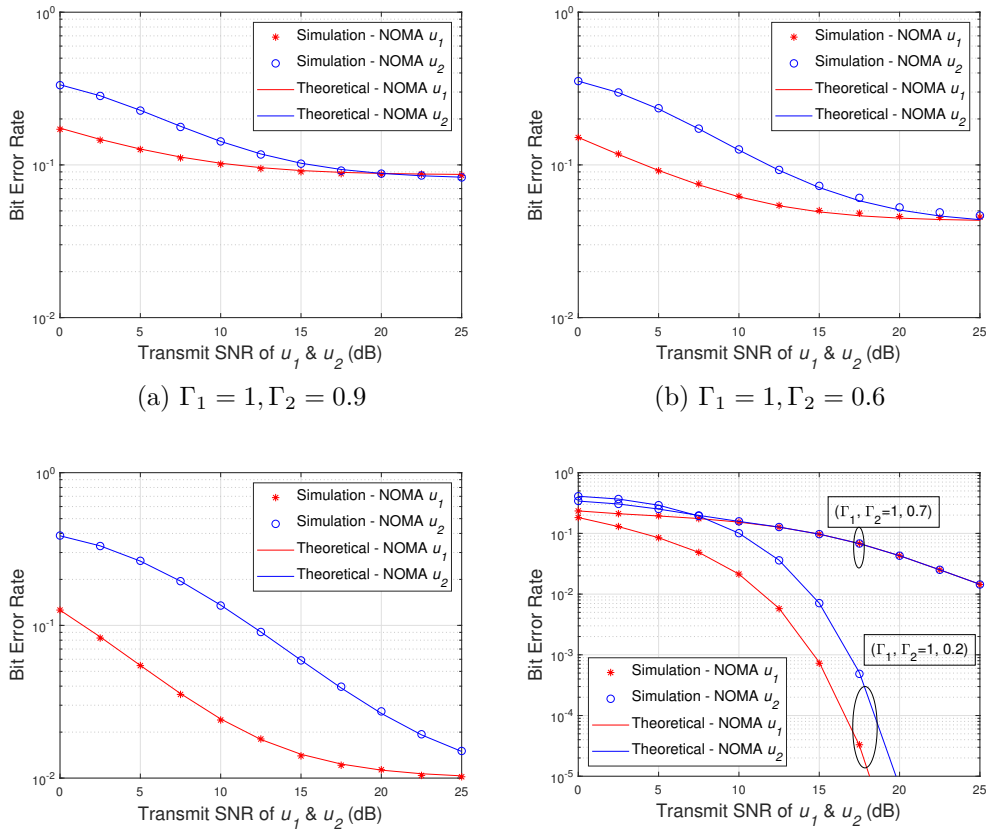

(a) $\Gamma_1 = 1, \Gamma_2 = 0.9$ (b) $\Gamma_1 = 1, \Gamma_2 = 0.6$

(c) $\Gamma_1 = 1, \Gamma_2 = 0.3$ (d) $\Gamma_1 = 1, \Gamma_2 = 0.7, 0.2$

Figure 6.1: BER plots of BSN-1 and BSN-2 for fading ($m_1 = 4, \Omega_1 = 1, m_2 = 1, \Omega_2 = 0$) and fading-free scenarios.

6.0.1 Analysis Validation

In Fig. 6.1, numerical and simulated BER of the NOMA enhanced BackCom system is plotted against transmit SNR of both BSNs. A Nakagami-m fading channel ($m_1 = 4, \Omega_1 = 1$) and a Rayleigh fading channel ($m_2 = 1, \Omega_2 = 1$) is taken in Fig. 6.1(a), 6.1(b) and 6.1(c) for the fading scenario of BSN-1 and BSN-2, respectively. Three different pairs of reflection coefficient values (Γ_1, Γ_2) are considered for the analysis. As can be seen from the figure, numerical results obtained using (5.18) and (5.29) match the simulation results for

different pairs of Γ_1 and Γ_2 values thus validating the theoretical analysis. It can also be observed that a larger separation in reflection coefficient values results in better BER behavior for NOMA enhanced BackCom. This is because, by lowering Γ_2, the IUI experienced by BSN-1 is decreased, resulting in better BER performance of BSN-1 due to the efficient utilization of the NOMA principle. As the BER performance of BSN-2 depends on the successful SIC operation of BSN-1, therefore, lowering the IUI indirectly influences the performance of BSN-2 as evident from its improved performance.

The BER plots are also given in Fig. 6.1(d) for a fading-free scenario by taking an arbitrarily large value of m_1 and m_2 to simulate a pure AWGN channel. The fading-free scenario provides a significant improvement in BER performance. Furthermore, similar behavior of larger separation resulting in better performance is also observed in fading-free scenarios.

6.0.2 Effects of the reflection coefficients

In Fig. 6.2, we investigate the effect of reflection coefficient on the normalized average of total effectively decoded bits of u_1 and u_2. The total effectively decoded bits correspond to the non-erroneous transmission of BSNs' bits over the total number of bits transmitted by BSN-1 and BSN-2. It is assumed that the reflection coefficient for the BSN-1, Γ_1, is set as 0.7 for the analysis. The results are plotted for three values of transmit SNRs, i.e., 0, 10, and 20 dB.

From Fig. 6.2, we can observe that the total normalized effective bits of u_1 and u_2 decrease with an increase in Γ_2 value. Therefore, the system

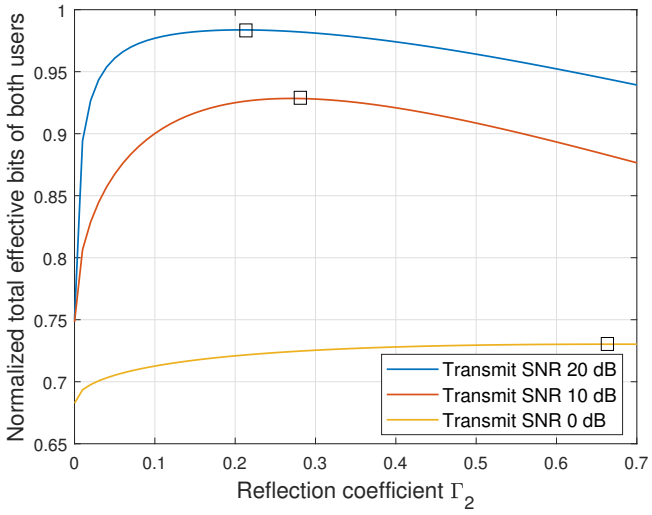

Figure 6.2: The normalized average of effectively decoded bits for BSN-1 and BSN-2 against Γ_2 while $\Gamma_1 = 0.7$.

performance is improved by setting a low value of Γ_2. This is again because, by setting a low value of Γ_2, the interference experienced by BSN-1 is reduced, thus, its BER performance is improved resulting in the greater non-erroneous transmission of bits by the system. However, it is to be noted from figure, that Γ_2 has a minimum value below which the performance of the system starts to degrade as BSN-2 is not able to decode itself at such a small value resulting in higher transmission errors.

The Γ_2 values are also marked for each transmit SNR which provides the best system performance in terms of the effective bits transmitted. For transmit SNRs of 0, 10, and 20 dBs, the optimal Γ_2 is 0.67, 0.27 and 0.21, respectively. It is evident from the fact that by lowering the transmit SNR, a greater Γ_2 value is needed by BSN-2 to decode itself successfully. We also find that the maximum normalized total effective bits turns out to be 0.9791 for the 20 dB SNR scenario.

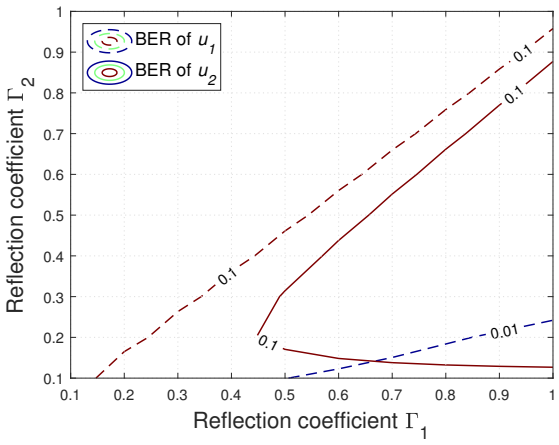

(a) Fading with transmit SNR = 15 dB

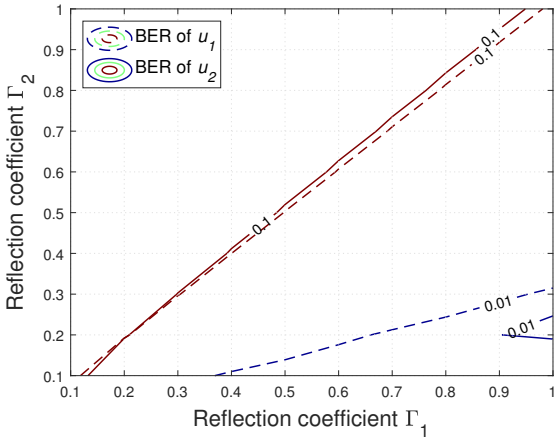

(b) Fading with transmit SNR = 20 dB

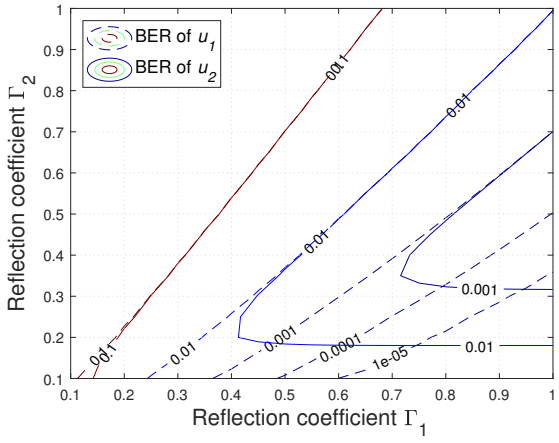

(c) Fading-free with transmit SNR = 15 dB

Figure 6.3: BER contour plot of BSN-1 and BSN-2 by varying Γ_1 and Γ_2 values for fading and fading-free scenarios

In Fig. 6.3, a contour plot of BER is plotted by varying the reflection coefficient pair of BSN-1 and BSN-2. The reflection coefficients of both BSNs are varied from 0.01 to a maximum value of 1 by always keeping $\Gamma_1 > \Gamma_2$ as found from the previous result in Fig. 6.1. The BER of BSN-1 is represented by a dotted line while the BER of BSN-2 is represented by a solid line. It can be observed from the contour plot that for any specific value of Γ_1, there exists a range of Γ_2 values smaller than Γ_1 for which we can achieve acceptable performance in a NOMA-BackCom system. For the fading case (see Fig. 6.3(a) and 6.3(b)), it can be observed that very little improvement is possible in BER unless either the transmit SNR is increased by placing the BSNs closer to CE or fading channel condition is boosted by removing obstructions in line-of-sight (LoS) path. The contour plots of the fading-free case is plotted in Fig. 6.3(c) for improvement comparison due to less channel severity.

6.0.3 Effect of the Nakagami-m fading parameter

Now, we investigate the impact of the fading parameter m on the BER performance of each BSN for a NOMA-BackCom system with two different sets of reflection coefficients. The BER plots are shown in Fig. 6.4 for transmit SNRs of u_1 and u_2 as 20 and 15 dBs, respectively. As can be observed from figure, the BER performance of both users depend strongly on the fading parameters of the channel. It can be seen that for suitable reflection coefficient pairs, the fading parameters affects the performance of BSN-1 more than BSN-2.

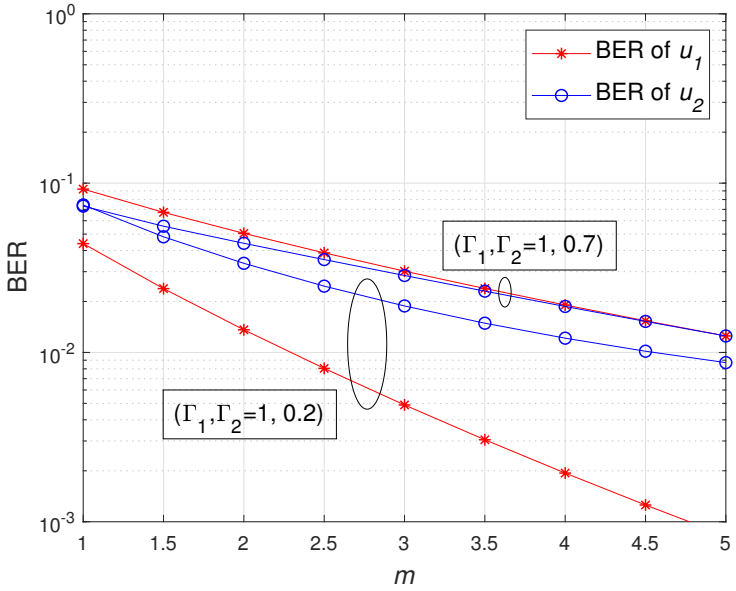

Figure 6.4: BER plots of BSN-1 and BSN-2 for various m values.

6.0.4 Comparison with OMA-TDMA scheme

In this section, we compare the performance of the NOMA-BackCom system with an OMA-TDMA transmission scheme in a BackCom system. Fig. 6.5 illustrates the increase in effective non-erroneous bits transmission by employing the NOMA scheme in a BackCom system of a single cluster with two BSNs as compared to an OMA-TDMA transmission scheme with two BSNs. It can be observed that the NOMA scheme indeed outperforms the OMA scheme due to the simultaneous transmission of two bits to the reader in a single time slot even though the OMA-TDMA scheme experiences no IUI from the second BSN. Individually, the TDMA BSN always has better BER performance as compared to NOMA BSN, i.e., a TDMA user has a greater number of successful transmissions as shown in Fig. 6.5 (b). However, the combined performance of NOMA scheme is better as the time spent by BSN

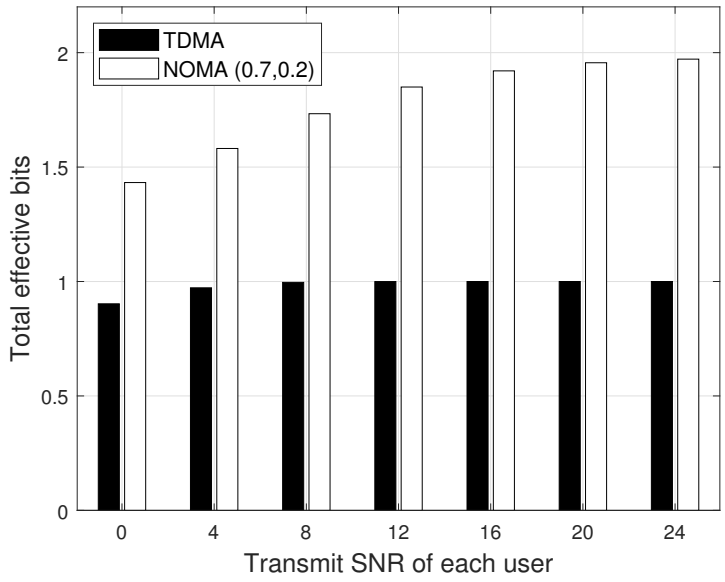

(a) Comparison of total effective bits

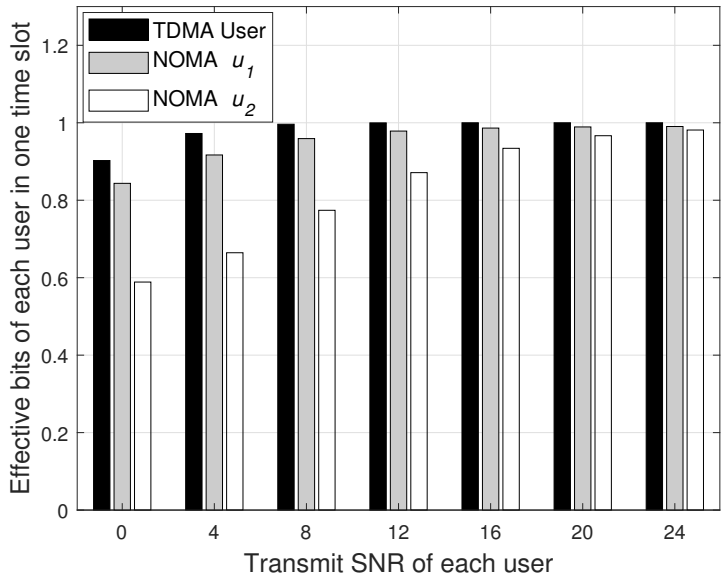

(b) Comparison of individual effective bits

Figure 6.5: Comparison of normalized effective bits transmitted of a NOMA-BackCom system ($\Gamma_1 = 0.7, \Gamma_2 = 0.2$) against OMA-TDMA scheme.

on each time slot is doubled under NOMA scheme as compared to TDMA scheme. At high SNR though, the BER difference between an individual NOMA and TDMA user becomes negligible.

Chapter 7

Conclusion & Future Works

7.1 Concluding notes

This work has presented the design and analysis of a NOMA enhanced bistatic BackCom system for a battery-less smart communication paradigm employed in an IoT scenario. We have derived the closed-form BER expressions for a cluster of two BSNs with imperfect SIC under Nakagami-m fading channel. Furthermore, the PDFs of the sum and difference of two i.n.i.d Nakagami-m distributions are also accurately approximated. All the derived expressions are verified with the simulations under different scenarios. Based on these expressions, we have evaluated the performance of the system in terms of the reflection coefficients. We have also found that the increment of SNR with unsuitable reflection coefficients does not lead to a better system performance, hence highlighting the significance of setting proper reflection coefficients according to the scenario. This necessitates an optimization study as a future work where reflection coefficients can be

optimized such that the system performance in terms of BER or effective transmitted bits can be improved. Further future extensions include BER analysis for higher modulation schemes with a higher number of BSNs in different fading environments.

7.2 Future Works

The proposed approach can be followed to multipler BSNs multiplexed by a single reader. As we have only carried out the study for only two users. Moreover, future extensions include BER analysis for higher modulation schemes in different fading environments. Another interesting problem is the optimization problem of selecting the most optimum reflection coefficients for the best system performance in terms of BER.

Bibliography

[1] M. Series, "IMT Vision–Framework and overall objectives of the future development of IMT for 2020 and beyond," 2015.

[2] J. G. Andrews, S. Buzzi, W. Choi, S. V. Hanly, A. Lozano, A. C. Soong, and J. C. Zhang, "What will 5G be?" *IEEE Journal on selected areas in communications*, vol. 32, no. 6, pp. 1065–1082, 2014.

[3] S. K. Routray and K. Sharmila, "4.5 G: A milestone along the road to 5G," in *2016 International Conference on Information Communication and Embedded Systems (ICICES)*. IEEE, 2016, pp. 1–6.

[4] M. Jaber, M. A. Imran, R. Tafazolli, and A. Tukmanov, "5G backhaul challenges and emerging research directions: A survey," *IEEE access*, vol. 4, pp. 1743–1766, 2016.

[5] Y. Tao, L. Liu, S. Liu, and Z. Zhang, "A survey: Several technologies of non-orthogonal transmission for 5G," *China Communications*, vol. 12, no. 10, pp. 1–15, 2015.

[6] R. I. Ansari, C. Chrysostomou, S. A. Hassan, M. Guizani, S. Mumtaz, J. Rodriguez, and J. J. Rodrigues, "5G D2D networks: Techniques,

challenges, and future prospects," *IEEE Systems Journal*, no. 99, pp. 1–15, 2017.

[7] M. Shafi, A. F. Molisch, P. J. Smith, T. Haustein, P. Zhu, P. De Silva, F. Tufvesson, A. Benjebbour, and G. Wunder, "5G: A tutorial overview of standards, trials, challenges, deployment, and practice," *IEEE Journal on Selected Areas in Communications*, vol. 35, no. 6, pp. 1201–1221, 2017.

[8] S. Zeb, A. Mahmood, S. A. Hassan, S. H. Ahmed, and M. Gidlund, "Impact of Indoor Multipath Channels on Timing Advance for URLLC in Industrial IoT," in *2020 IEEE International Conference on Communications Workshops (ICC Workshops)*, 2020, pp. 1–6.

[9] S. Zeb, A. Mahmood, H. Pervaiz, S. A. Hassan, M. I. Ashraf, Z. Li, and M. Gidlund, "On TOA-based Ranging over mmWave 5G for Indoor Industrial IoT Networks," in *2020 IEEE Globecom Workshops (GC Wkshps*, 2020, pp. 1–6.

[10] A. H. Ngu, M. Gutierrez, V. Metsis, S. Nepal, and Q. Z. Sheng, "IoT middleware: A survey on issues and enabling technologies," *IEEE Internet of Things Journal*, vol. 4, no. 1, pp. 1–20, 2017.

[11] M. R. Palattella, M. Dohler, A. Grieco, G. Rizzo, J. Torsner, T. Engel, and L. Ladid, "Internet of things in the 5G era: Enablers, architecture, and business models," *IEEE Journal on Selected Areas in Communications*, vol. 34, no. 3, pp. 510–527, 2016.

[12] Q. Abbas, S. Zeb, and S. A. Hassan, "Age of Information in Backscatter Communication," in *Wireless-Powered Backscatter Communications for Internet of Things*. Springer, pp. 67–80.

[13] Q. Abbas, S. Zeb, S. A. Hassan, R. Mumtaz, and S. A. R. Zaidi, "Joint optimization of Age of Information and Energy Efficiency in IoT Networks," in *2020 IEEE 91st Vehicular Technology Conference (VTC2020-Spring)*, 2020, pp. 1–5.

[14] L. Wan, Z. Guo, Y. Wu, W. Bi, J. Yuan, M. Elkashlan, and L. Hanzo, "4G\/5G Spectrum Sharing: Efficient 5G Deployment to Serve Enhanced Mobile Broadband and Internet of Things Applications," *ieee vehicular technology magazine*, vol. 13, no. 4, pp. 28–39, 2018.

[15] Z. Dawy, W. Saad, A. Ghosh, J. G. Andrews, and E. Yaacoub, "Toward massive machine type cellular communications," *IEEE Wireless Communications*, vol. 24, no. 1, pp. 120–128, 2016.

[16] F. Jejdling, "Ericsson Mobility Report," Tech. Rep., Nov 2019, accessed on: Nov. 13, 2020. [Online]. Available: ericsson.com/4acd7e/assets/local/mobility-report/documents/2019/november-2019.pdf

[17] L. Da Xu, W. He, and S. Li, "Internet of things in industries: A survey," *IEEE Transactions on industrial informatics*, vol. 10, no. 4, pp. 2233–2243, 2014.

[18] E. Sisinni, A. Saifullah, S. Han, U. Jennehag, and M. Gidlund, "Industrial internet of things: Challenges, opportunities, and directions," *IEEE*

Transactions on Industrial Informatics, vol. 14, no. 11, pp. 4724–4734, 2018.

[19] Q. Wu, G. Y. Li, W. Chen, D. W. K. Ng, and R. Schober, "An overview of sustainable green 5G networks," *IEEE Wireless Communications*, vol. 24, no. 4, pp. 72–80, 2017.

[20] C. H. News, "Tsunami of data could consume one-fifth of global electricity by 2025." Tech. Rep., Nov 2019. [Online]. Available: climatechangenews.com/

[21] F. Jejdling, "Ericsson Mobility Report," Tech. Rep., June 2020, accessed on: Nov. 13, 2020. [Online]. Available: ericsson.com/4acd7e/assets/local/mobility-report/documents/2020/June-2020.pdf

[22] D. Niyato, D. I. Kim, M. Maso, and Z. Han, "Wireless powered communication networks: Research directions and technological approaches," *IEEE Wireless Communications*, vol. 24, no. 6, pp. 88–97, 2017.

[23] A. Bletsas, P. N. Alevizos, and G. Vougioukas, "The art of signal processing in backscatter radio for μW (or less) internet of things: intelligent signal processing and backscatter radio enabling batteryless connectivity," *IEEE Signal Processing Magazine*, vol. 35, no. 5, pp. 28–40, 2018.

[24] X. Lu, D. Niyato, H. Jiang, D. I. Kim, Y. Xiao, and Z. Han, "Ambient backscatter assisted wireless powered communications," *IEEE Wireless Communications*, vol. 25, no. 2, pp. 170–177, 2018.

[25] W. Liu, K. Huang, X. Zhou, and S. Durrani, "Next generation backscatter communication: systems, techniques, and applications," *EURASIP Journal on Wireless Communications and Networking*, vol. 2019, no. 1, pp. 1–11, 2019.

[26] C. Xu, L. Yang, and P. Zhang, "Practical backscatter communication systems for battery-free Internet of Things: A tutorial and survey of recent research," *IEEE Signal Processing Magazine*, vol. 35, no. 5, pp. 16–27, 2018.

[27] X. Lu, D. Niyato, H. Jiang, D. I. Kim, Y. Xiao, and Z. Han, "Ambient backscatter assisted wireless powered communications," *IEEE Wireless Communications*, vol. 25, no. 2, pp. 170–177, 2018.

[28] N. Van Huynh, D. T. Hoang, X. Lu, D. Niyato, P. Wang, and D. I. Kim, "Ambient backscatter communications: A contemporary survey," *IEEE Communications Surveys & Tutorials*, vol. 20, no. 4, pp. 2889–2922, 2018.

[29] J. Kimionis, A. Bletsas, and J. N. Sahalos, "Increased range bistatic scatter radio," *IEEE Transactions on Communications*, vol. 62, no. 3, pp. 1091–1104, 2014.

[30] P. N. Alevizos, K. Tountas, and A. Bletsas, "Multistatic scatter radio sensor networks for extended coverage," *IEEE Transactions on Wireless Communications*, vol. 17, no. 7, pp. 4522–4535, 2018.

[31] X. Lu, P. Wang, D. Niyato, D. I. Kim, and Z. Han, "Wireless charging technologies: Fundamentals, standards, and network applications,"

IEEE Communications Surveys & Tutorials, vol. 18, no. 2, pp. 1413–1452, 2016.

[32] Z. Ding, X. Lei, G. K. Karagiannidis, R. Schober, J. Yuan, and V. K. Bhargava, "A survey on non-orthogonal multiple access for 5G networks: Research challenges and future trends," *IEEE Journal on Selected Areas in Communications*, vol. 35, no. 10, pp. 2181–2195, 2017.

[33] V. Basnayake, D. N. K. Jayakody, V. Sharma, N. Sharma, P. Muthuchidambaranathan, and H. Mabed, "A new green prospective of non-orthogonal multiple access (noma) for 5g," *Information*, vol. 11, no. 2, p. 89, 2020.

[34] C. Psomas and I. Krikidis, "Backscatter communications for wireless powered sensor networks with collision resolution," *IEEE Wireless Communications Letters*, vol. 6, no. 5, pp. 650–653, 2017.

[35] J. Guo, X. Zhou, S. Durrani, and H. Yanikomeroglu, "Design of non-orthogonal multiple access enhanced backscatter communication," *IEEE Transactions on Wireless Communications*, vol. 17, no. 10, pp. 6837–6852, 2018.

[36] S. Zeb, Q. Abbas, S. A. Hassan, A. Mahmood, R. Mumtaz, S. H. Zaidi, S. A. R. Zaidi, and M. Gidlund, "NOMA enhanced backscatter communication for green IoT networks," in *2019 16th International Symposium on Wireless Communication Systems (ISWCS)*. IEEE, 2019, pp. 640–644.

[37] F. Jameel, S. Zeb, W. U. Khan, S. A. Hassan, Z. Chang, and J. Liu, "NOMA-Enabled Backscatter Communications: Toward Battery-Free IoT Networks," *IEEE Internet of Things Magazine*, vol. 3, no. 4, pp. 95–101, 2020.

[38] S. Zeb, Q. Abbas, S. A. Hassan, A. Mahmood, and M. Gidlund, "Enhancing Backscatter Communication in IoT Networks with Power-Domain NOMA," in *Wireless-Powered Backscatter Communications for Internet of Things*. Springer, 2021, pp. 81–101.

[39] C.-B. Le and D.-T. Do, "Outage performance of backscatter NOMA relaying systems equipping with multiple antennas," *Electronics Letters*, vol. 55, no. 19, pp. 1066–1067, 2019.

[40] G. Yang, X. Xu, and Y.-C. Liang, "Resource allocation in NOMA-enhanced backscatter communication networks for wireless powered IoT," *IEEE Wireless Communications Letters*, vol. 9, no. 1, pp. 117–120, 2019.

[41] Y. Liao, G. Yang, and Y.-C. Liang, "Resource allocation in NOMA-enhanced full-duplex symbiotic radio networks," *IEEE Access*, vol. 8, pp. 22 709–22 720, 2020.

[42] Q. Zhang, L. Zhang, Y.-C. Liang, and P.-Y. Kam, "Backscatter-NOMA: A symbiotic system of cellular and Internet-of-Things networks," *IEEE Access*, vol. 7, pp. 20 000–20 013, 2019.

[43] B. Lyu, Z. Yang, G. Gui, and H. Sari, "Optimal time allocation in backscatter assisted wireless powered communication networks," *Sensors*, vol. 17, no. 6, p. 1258, 2017.

[44] B. Lyu, Z. Yang, H. Guo, F. Tian, and G. Gui, "Relay cooperation enhanced backscatter communication for Internet-of-Things," *IEEE Internet of Things Journal*, vol. 6, no. 2, pp. 2860–2871, 2019.

[45] A. Farajzadeh, O. Ercetin, and H. Yanikomeroglu, "UAV data collection over NOMA backscatter networks: UAV altitude and trajectory optimization," in *ICC 2019-2019 IEEE International Conference on Communications (ICC)*. IEEE, 2019, pp. 1–7.

[46] Proakis, *Digital Communications 5th Edition*. McGraw Hill, 2007.

[47] A. Annamalai, C. Tellambura, and V. K. Bhargava, "Equal-gain diversity receiver performance in wireless channels," *IEEE Transactions on Communications*, vol. 48, no. 10, pp. 1732–1745, 2000.

[48] M. A. Rahman and H. Harada, "New exact closed-form PDF of the sum of Nakagami-m random variables with applications," *IEEE Transactions on Communications*, vol. 59, no. 2, pp. 395–401, 2010.

[49] M. Nakagami, "The m-distribution—A general formula of intensity distribution of rapid fading," in *Statistical methods in radio wave propagation*. Elsevier, 1960, pp. 3–36.

[50] F. J. Massey Jr, "The Kolmogorov-Smirnov test for goodness of fit," *Journal of the American statistical Association*, vol. 46, no. 253, pp. 68–78, 1951.

[51] M. K. Simon and M.-S. Alouini, *Digital communication over fading channels*. John Wiley & Sons, 2005, vol. 95.

[52] F. Crimins, "Numerical recipes in C++: The art of scientific computing," *Applied Biochemistry and Biotechnology*, vol. 104, no. 1, p. 95, 2003.